



Sjoerd Broekhuijsen

# $^{11}\text{B}_4\text{C}$ containing neutron multilayers

Thesis submitted for licentiate degree

Thin Film Physics  
IFM



2021



In such ugly times, the only true  
protest is beauty.

---

Phil Ochs



# Abstract

The work in this thesis covers the design, growth and characterisation of neutron multilayers. The performance of these multilayers is highly dependent on the obtained interface width between the layers, even a modest improvement can offer a substantial increase in reflectivity performance. As multilayers are such an integral component of many neutron optical instruments, any improvement in terms of reflectivity performance has broad implications for all neutron scattering experiments. This project has been carried out with the construction of the European Spallation Source (ESS) in mind, but the principles extend to all neutron scattering sources.

The samples that have been deposited in this work primarily consist of Ni/Ti multilayers that were co-deposited with  $^{11}\text{B}_4\text{C}$  using ion assisted magnetron sputter deposition. Much of the focus in this work lies on the simulation of the reflectivity performance of these multilayers. Structural parameters have been obtained by fitting experimental neutron and X-ray data simultaneously to simulated models. Additional measurements have been performed using TEM to confirm these results and XPS and ERDA to obtain compositional information.

The fits to the experimental data suggest a significant improvement in interface width for the samples that have been co-deposited with  $^{11}\text{B}_4\text{C}$  using a split-bias scheme during deposition. Any accumulation of roughness has been eliminated, and the overall interface width has been reduced from 6.5 Å to 4.5 Å per bilayer (check this). The respective reflectivity performance for these structural parameters have been simulated for a neutron supermirror ( $N = 5000$ ) for both materials at a neutron wavelength at  $\lambda = 3 \text{ \AA}$  using the IMD software. At an angle of 1.8 °, this results in a predicted reflectivity increase from 60% to 70% (check numbers) for the pure Ni/Ti and the sample that has been co-deposited with  $^{11}\text{B}_4\text{C}$  respectively.



# Preface

This is where I will include my acknowledgements and such. I may start with a short background (one small paragraph) where I also mention SwedNess and what not. I will probably write this "chapter" last.

# Contents

<b>Abstract</b>	<b>iii</b>
<b>Preface</b>	<b>v</b>
<b>Contents</b>	<b>vi</b>
<b>1 Introduction</b>	<b>1</b>
1.1 Background . . . . .	1
1.2 European Spallation Source . . . . .	2
1.3 Neutron multilayers . . . . .	3
1.4 Research aims . . . . .	4
1.5 Outline of the thesis . . . . .	4
<b>2 Scattering Theory</b>	<b>5</b>
2.1 Neutron scattering . . . . .	5
2.2 Neutron scattering length . . . . .	8
2.3 Choice of materials . . . . .	14
2.4 Neutron scattering in reciprocal space . . . . .	14
<b>3 Multilayer and supermirror optics</b>	<b>21</b>
3.1 Reflectivity from different interfaces . . . . .	21
3.2 Interface imperfections . . . . .	26
3.3 Off-specular scattering . . . . .	27
<b>4 Multilayer Depositions</b>	<b>33</b>
4.1 Magnetron sputter deposition . . . . .	33
4.2 Ion Assistance . . . . .	35
4.3 $^{11}\text{B}_4\text{C}$ co-deposition . . . . .	37
4.4 Reducing interface width . . . . .	37
4.5 Deposition system at PETRA III . . . . .	38
<b>5 Instrumental aspects</b>	<b>39</b>
5.1 Neutron Reflectometry . . . . .	39
5.2 X-ray Reflectometry . . . . .	40

5.3	The beam overspill effect . . . . .	42
<b>6</b>	<b>Reflectivity Simulations</b>	<b>45</b>
6.1	Parrat recursion . . . . .	45
6.2	Born Approximation . . . . .	46
6.3	Sample description . . . . .	48
<b>7</b>	<b>Multilayer Characterization</b>	<b>51</b>
7.1	Elastic Recoil Detection Analysis . . . . .	51
7.2	X-ray Photoelectron Spectroscopy . . . . .	51
7.3	Transmission Electron Microscopy . . . . .	52
<b>8</b>	<b>Summary of the results</b>	<b>57</b>
8.1	Pure Ni/Ti multilayers . . . . .	57
8.2	Ni/Ti multilayers containing $^{11}\text{B}_4\text{C}$ . . . . .	58
<b>9</b>	<b>Outlook</b>	<b>61</b>
9.1	Ni/Ti multilayers . . . . .	61
9.2	Co/Ti multilayers . . . . .	61
<b>10</b>	<b>Summary of the papers</b>	<b>63</b>
10.1	Paper I . . . . .	63
10.2	Paper II . . . . .	63
<b>Bibliography</b>		<b>65</b>
<b>Papers</b>		<b>69</b>



# Chapter 1

## Introduction

### 1.1 Background

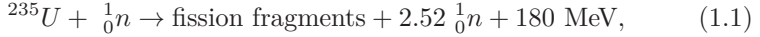
Neutron scattering is a versatile non-destructive experimental technique to study the structure and dynamics of materials. The technique is used by over 5000 researchers over the world [1] spanning over an increasingly large range of disciplines, including physics, chemistry, biology, ceramics and metallurgy [2]. Neutron scattering differentiates itself from X-ray scattering due to the interaction with the investigated material. While X-rays interact with the electron cloud, neutrons interact with the nucleus of the atom. This gives several distinct advantages for neutron scattering. As the nucleus of an atom is only a tiny portion of the atom, most of the material will be empty space to a neutron. Because of this, neutrons have a very large penetration depth [3], making it possible to study bulk materials. Moreover, the wavelength of neutrons is similar to the atomic spacing in solids, making it ideal for structural studies [4]. Another advantage of neutron scattering arises from the fact that neutrons carry a magnetic dipole moment, the interaction of the neutron's spin with unpaired electrons gives rise to magnetic scattering [5]. The scattering properties for neutrons vary seemingly randomly across the periodic table, even different isotopes of the same element can have completely different properties for neutrons. This makes the combination X-ray and neutron scattering a very powerful technique, as the scattering properties for X-rays are dependent on the atomic number. By combining these two techniques, it is possible to obtain two completely independent data sets with the same structural information. This latter advantage is exploited in this report, where a combination of neutron and X-ray scattering is used to find the structural properties of deposited multilayers.

The dawn of neutron scattering began in the first half of the twentieth century. The first experiments on Bragg reflection using neutrons were performed as early as 1936, however it wasn't until the second half of the 1940s that the invention of the nuclear reactor made the first proper neutron experiments possible [6]. As free neutrons have a mean lifetime of 15 minutes [4], they need to be produced while running the experiment. Traditionally, free neutrons for scientific experiments are produced at fission reactors. In this process, a neutron collides with uranium-235, forming the following

## 1. Introduction

---

nuclear reaction:



releasing two or three free neutrons carrying an energy of 1.29 MeV [4], averaging to 2.52 free neutrons after each collision. Each emitted neutron can undergo a fission reaction with another  $^{235}\text{U}$  particle forming a chain reaction where even more free neutrons are emitted. This technique has however reached its technological limits in terms of neutron flux due to power density problems in the reactor core [7][8], but also the risk of nuclear proliferation has made the enrichment of  $^{235}\text{U}$  a politically difficult matter [8]. A slightly newer technique that does not have this disadvantage is the use of spallation sources. In these sources, proton pulses are accelerated to high energies, typically in the range of GeV, and directed onto a target. Depending on the target material, up to 50 neutrons can be released per spallation event [4], making an extremely high peak flux of neutrons possible. For both of these techniques, the energy of the neutrons is too high to be used for experiments, with energies that correspond to a wavelength in the order of  $\lambda = 10^{-5} \text{ \AA}$  [4]. In order to reduce the energy of the neutron beam, the neutrons are transferred through a moderator material such as  $\text{H}_2\text{O}$ . This slows the neutrons down, and thereby reduces their energy such that they can be used for neutron scattering experiments. Finally, neutrons need to be brought from the source to experiments. As neutrons do not have any charge, they cannot be bent by any electromagnetic field. Instead, neutron mirrors are used that enclose the flight path of neutrons [9].

## 1.2 European Spallation Source

As this project is part of the SwedNess neutron graduate school, it should be seen in context of the construction of the European Spallation Source (ESS), which is being built in Lund. An overarching goal of SwedNess in general is to develop an understanding of neutron scattering in particular and thereby increasing the expertise that is needed with planned operations of ESS in the future. The spallation source is designed to deliver 5 MW of 2.5 GeV protons to a single target, which corresponds to an increase in average and peak neutron flux by a factor of 30 compared to the currently most powerful pulsed spallation source at ISIS in the UK [10]. The aim of ESS is to deliver a time average flux of neutrons that is comparable to the brightest continuous source in existence at ILL, using a low enough pulse repetition rate such in order to avoid loss of efficiency at high flux even

for cold neutrons applications [11]. Construction started at 2014, with full operational performance planned in 2025 [11]

### 1.3 Neutron multilayers

Neutron multilayers are used in many different neutron optical instruments. A common example is that of neutron guides, which are necessary to guide a neutron beam from source to experiment. In a neutron guide, different neutron supermirrors are used to enclose the beam trajectory, these neutron supermirrors consist of multilayers with many different periods. Multilayers are also used for monochromators, which are used to select specific wavelengths of a beam. By choosing a certain period at a specified angle, only one wavelength fulfils the Bragg condition at reflection. Therefore, only a certain wavelength will be reflected at the specified angle. This technique is commonly used to filter specific wavelengths. Magnetic multilayers can be used to create neutron polarisers. The total neutron scattering potential has a contribution from the nuclear and magnetic scattering length, whether the magnetic scattering length subtracts or adds to the total scattering length depends on the polarisation state of the incoming neutron beam [5]. Using the right set of materials, the scattering contrast will disappear for one spin-state only, making the multilayer transparent for that spin-state while the other spin-state is reflected. These polarised neutron beams are used to investigate magnetic properties of materials. Interface width of multilayers and the current state-of-the-art The performance of such multilayer components in terms of reflected intensity is highly dependent on both the scattering contrast and the interface width between the layers. The scattering contrast is limited by the materials of choice, while the interface width can be reduced using the correct deposition techniques. Reducing this interface width offers great possibilities in terms of performance for multilayer components. The obtained reflectivity depends exponentially on the achieved interface width. Meaning even a small improvement will lead to a drastic increase in reflectivity performance. This means that the total flux at experiment can be increased very significantly by improving the instrumentation, without the need of more power-intensive neutron sources. Another advantage of a reduced interface width is that the minimum thickness that can be achieved is reduced as well. The total thickness of a layer cannot meaningfully be less than the width of the interfaces. If the interfaces can be made flatter and more abrupt, the layers can be made thinner as well. This makes it possible for instance to deposit monochromators that can be applied for higher wavelengths and lower energies, such as cold neutron beams.

## 1.4 Research aims

The essential goal of this work is to enhance the performance of neutron multilayers by reducing the interface width between the layers. The biggest improvement in terms of neutron flux at experiment is not expected to come from more brilliant neutron sources, but instead from the improvement of different neutron optical components [12]. As multilayers are such essential and crucial elements in any of the intended neutron instrumentation, even the slightest improvements of the performance will have an immediate and large impact on all research conducted using those instruments. The work presented will have a significant focus on the simulation and modelling of neutron multilayers. The underlying goal here is to develop an understanding of the interface evolution of the samples, and how their performance is affected by different parameters.

## 1.5 Outline of the thesis

This thesis will start with a theoretical background behind this work. Starting with chapter 2, the general scattering theory will be described. In this chapter, the underlying concepts will be explained in a general way. The optical theory that is used for the scattering experiments is described in chapter 3, where diffraction for different multilayers are explained. The deposition of the multilayers in this work is covered in chapter 4. This chapter will also describe the sputtering techniques, and how these are used to minimize the interface width between the individual layers. The instrumental aspects for the reflectivity are described in chapter 5, where both neutron and X-ray reflectometry will be described. The theory behind the reflectivity simulations that are used for the characterization of structural parameters is described in chapter 6. The other techniques that have been used for multilayer characterizations are covered in chapter 7. A summary of the results will be given in chapter 8, followed by an outlook in chapter 9. The summary of the papers in this work is covered in chapter 10, while the papers themselves can be found after the bibliography.

# Chapter 2

## Scattering Theory

### 2.1 Neutron scattering

Neutron scattering may be understood when we consider how the Schrödinger wave equation can be applied to particles as well. Similar to the better-known case of photons, a beam of neutrons can either be described as a wave or as particles. While we intuitively think of neutrons as real particles with a very small but finite radius, the wavelength of a neutron can in principle have any size, even in the order of whole meters. From this realization of neutrons as a wave, it follows that the equations for diffraction of X-rays are directly applicable to neutrons as well. So while we may focus on neutrons, the principles in these sub-chapters apply to X-ray waves as well. In order to fully understand what happens when a neutron beam scatters from an interface, we consider an incoming neutron beam towards a surface with a certain scattering potential  $V_0$ , as illustrated in figure 2.1. The neutron wave can be described by Schrödinger's equation as usual:

$$\left( \frac{\hbar^2}{2m} \nabla^2 + V(r) \right) \Psi(r) = E\Psi(r) \quad (2.1)$$

The energy of the neutron is denoted by  $E$ , while  $V$  describes the potential to which the neutron is subject to, which may be described by the following expression [13]:

$$V(r) = \frac{2\pi\hbar}{m} N_b \quad (2.2)$$

The factor  $N_b$  denotes the scattering length density (SLD) and can be seen as a measure of the scattering power for a certain material. This quantity will be further elaborated upon in subsection 2.2.2. For pedagogical reasons we assume that the scattering interface is perfectly flat and abrupt, meaning the only potential barrier in the sample is perpendicular to the surface. So in this case, only the normal component of the wave vector is affected by the potential barrier. And it is therefore the normal component of the neutron's kinetic energy that determines whether we get total reflection from the barrier. The wave vector  $\mathbf{k}_i$  of the incident wave can be expressed as

## 2. Scattering Theory

---

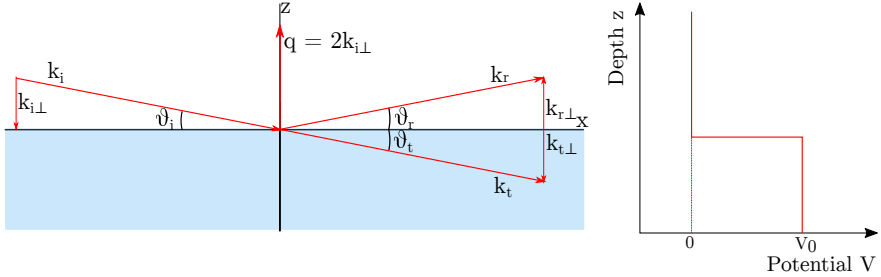


Figure 2.1: The neutron beam is subject to a potential barrier upon reflection at an interface. Part of the beam will be transmitted, while another part of the beam will be reflected.

usual from a finite potential:

$$\mathbf{k}_{i\perp} = \frac{\sqrt{2mE_{i\perp}}}{\hbar} = \mathbf{k}_i \sin \theta \quad (2.3)$$

So rewriting for the kinetic energy we get:

$$E_{i\perp} = \frac{(h\mathbf{k}_i \sin \theta_i)^2}{8\pi^2 m}. \quad (2.4)$$

If the perpendicular component of the kinetic energy,  $E_{i\perp} < V$ , then total reflection will occur, the critical angle is then given by  $E_{i\perp} = V$ . We can express the critical angle in wave vector transfer  $q$ . The wave vector  $k$  can simply be expressed as  $k = \frac{2\pi}{\lambda}$ , and since  $q = 2k_i \sin \theta_i$  we get:

$$q = \frac{4\pi}{\lambda} \sin \theta. \quad (2.5)$$

So using this in combination with equations 2.4 and 2.2 we get:

$$q_c = \sqrt{16\pi N_b}. \quad (2.6)$$

This interaction is generally considered elastic, therefore the normal part of the beam will be fully reflected with the same angle as the incoming beam meaning just as one would expect from a perfect mirror. This reflection where  $\theta_i = \theta_r$  is referred to as specular reflection.

If  $E_{i\perp} > V$ , the reflection is not total and part of the neutron beam will be transmitted through the interface. The transmitted beam will have its

kinetic energy reduced by the potential barrier, giving us  $E_t = E_i - V$ . So using this energy with the potential given in equation 2.2 we get:

$$\mathbf{k}_{t\perp}^2 = \frac{2m(E - V)}{\hbar^2} = \frac{2mE}{\hbar^2} - 4\pi N_b \quad (2.7)$$

$$\mathbf{k}_{t\perp}^2 = \mathbf{k}_{i\perp}^2 - 4\pi N_b \quad (2.8)$$

From this relation, it also follows that the potential barrier needs to be as large as possible to maximize the total reflection, as a lower potential barrier leads to a large part of the neutron wave being transmitted. We can also define our refractive index:

$$n^2 = \frac{\mathbf{k}_t^2}{\mathbf{k}_i^2} = \frac{\mathbf{k}_{t\parallel}^2 + (\mathbf{k}_{i\perp}^2 - 4\pi N_b)}{\mathbf{k}_i^2} = \frac{\mathbf{k}_{i\parallel}^2 + (\mathbf{k}_{i\perp}^2 - 4\pi N_b)}{\mathbf{k}_i^2} \quad (2.9)$$

Where we used  $\mathbf{k}_{i\parallel} = \mathbf{k}_{t\parallel}$ , as there's no potential barrier in the parallel direction. So filling in equation 2.8 we get:

$$n^2 = 1 - \frac{4\pi N_b}{\mathbf{k}_i^2} = 1 - \frac{\lambda^2 N_b}{2\pi} \quad (2.10)$$

For neutrons,  $n \approx 1$ , so the refractive index for neutrons is often given as:

$$n = 1 - \frac{\lambda^2 N_b}{2\pi} \quad (2.11)$$

### 2.1.1 Fresnel reflection

To get to an expression for the reflectivity after reflection, we consider the incoming neutron wave  $\Psi_i$ , hitting an interface with refractive index  $n$ , this results in a reflected and a transmitted wave which are denoted by  $\Psi_r$  and  $\Psi_t$  respectively. Considering the vertical component of the wave, that is in the z-direction, we can apply the boundary condition to get the following expression:

$$\Psi_0 = A_i \cdot e^{i \cdot \mathbf{k}_i \cdot \mathbf{z}} + A_r \cdot e^{-i \cdot \mathbf{k}_r \cdot \mathbf{z}} \quad (2.12)$$

$$\Psi_1 = A_t \cdot e^{i \cdot \mathbf{k}_{tz}} \quad (2.13)$$

From the boundary conditions at  $z = 0$ , we get:

$$A_i + A_r = A_t \quad (2.14)$$

$$A_i \cdot \mathbf{k}_i + A_r \cdot \mathbf{k}_r = A_t \cdot \mathbf{k}_t \quad (2.15)$$

## 2. Scattering Theory

---

For specular reflection,  $\theta_i = \theta_r$ , and for elastic scattering the wave vector is conserved, it does change direction however giving  $\mathbf{k}_r = -\mathbf{k}_i$  this gives us for the component that is perpendicular to the plane of incidence:

$$(\mathbf{A}_i - \mathbf{A}_r) \cdot \mathbf{k}_i = \mathbf{A}_t \cdot \mathbf{k}_t \quad (2.16)$$

Combining equations 2.14 and 2.16, we get:

$$\frac{\mathbf{A}_i - \mathbf{A}_r}{\mathbf{A}_i + \mathbf{A}_r} = \frac{\mathbf{k}_t}{\mathbf{k}_i} \quad (2.17)$$

Which we can rewrite using standard algebra as:

$$r = \frac{A_r}{A_i} = \frac{\mathbf{k}_i - \mathbf{k}_t}{\mathbf{k}_i + \mathbf{k}_t} \quad (2.18)$$

Where  $r$  represents the fraction of the incident beam that is reflected. Note that the intensity, which is what is actually being measured during an experiment, is given by  $r^2$ . Using equations 2.6, 2.8 and 2.18, we can re-write this in terms of  $q$  and  $q_c$ :

$$I = |r^2| = \left[ \frac{q - \sqrt{q^2 - q_c^2}}{q + \sqrt{q^2 - q_c^2}} \right]^2 \quad (2.19)$$

During experiments, one often uses the incident angle  $\theta_i$  instead of  $q$ . To get to the intensity in terms of the incidence angle  $\theta_i$  one can simply use equation 2.5 and put it into equation 2.19. At high angles of incidence, when  $q >> q_c$ , equation 2.19 reduces to:

$$I = \frac{16\pi}{q^4} N_b^2. \quad (2.20)$$

From which it follows that the intensity for a single layer falls off with  $q^4$  at higher angles, even for perfectly smooth interfaces. This expression is also used for the Born approximation, which will be covered later in subsection 6.2.

## 2.2 Neutron scattering length

While X-ray scattering comes from interaction with the electron cloud, neutron scattering can occur in two ways; nuclear scattering and magnetic scattering. Magnetic scattering occurs when unpaired electrons in a material

interact with the magnetic moment of the neutron, while nuclear scattering occurs due to interaction with the nucleus. In this work we will focus on nuclear scattering. The scattering of neutrons depends directly on the scattering potential between the nucleus and the neutron, denoted by  $V(r)$ . This interaction potential acts on an extremely short range and falls to zero in the order of 10-15 m. Since this is orders of magnitudes shorter than the typical wavelength of neutrons, which is in the order of 10-10 m, we can essentially describe the nucleus as a pure point scatterer. The incoming wave of neutrons can be described by a planar wave:

$$\Psi_i = e^{ikx} \quad (2.21)$$

where  $k$  is the wavenumber  $\frac{2\pi}{\lambda}$ , and  $x$  is the distance from the nucleus in the propagation direction. The scattered wave will be spherically symmetrical and can be described as:

$$\Psi_s = \frac{b}{r} e^{ikr} \quad (2.22)$$

where  $r$  is the radial distance to the nucleus, and  $b$  is the scattering length of the nucleus. The scattering length differs for each isotope in the periodic table and represents the strength of the neutron-nucleus interaction, the scattering length can basically be seen as the radius of the nucleus as experienced by the neutron. This gets intuitively clear when one thinks of the scattering length in the scattering cross section. The total scattering cross section is simply defined as the amount of neutrons scattered per second divided by the neutron flux:

$$\sigma_s = \frac{\text{Neutrons scattered per second}}{\Phi} \quad (2.23)$$

Where  $\Phi$  is the neutron flux, which describes the incident neutrons per unit area per second. As suggested by the name, the scattering cross section represents an area, and can be interpreted as a measure of the size of the nucleus as experienced by the neutron. We can calculate the scattering cross section by starting from the differential scattering cross section [1]:

$$\sigma_s = \frac{\text{Neutrons scattered per second into solid angle } \Omega}{\Phi} \quad (2.24)$$

The total scattering cross section is related to the differential cross section by:

$$\sigma_s = \int \frac{d\sigma}{d\Omega} d\Omega \quad (2.25)$$

## 2. Scattering Theory

---

We can calculate the neutron flux by multiplying the probability density function of the neutron wave  $|\Psi_i|^2$  by its velocity. For the incident neutron beam, this will simply be:

$$\Phi = v|\Psi_i|^2 = v \quad (2.26)$$

While the scattered neutron flux can be expressed by:

$$\Phi_s = v|\Psi_s|^2 = v \frac{b^2}{r^2} \quad (2.27)$$

To get to the amount of scattered neutrons per second that pass through an area  $dA$  we simply have to integrate over this area. Which leads to [14]:

$$v \frac{b^2}{r^2} dA = vb^2 d\Omega \quad (2.28)$$

As this quantity describes the amount of neutrons scattered per second into a solid angle, it is exactly equal to the numerator in the differential cross section as seen in equation 2.24 so plugging this in we get:

$$\frac{d\sigma}{d\Omega} d\Omega = \frac{vb^2 d\Omega}{\Phi d\Omega} = b^2 \quad (2.29)$$

Where we used the fact that the neutron velocity is equal to the neutron flux as seen in equation 2.26. To get to the total scattering cross section we have to integrate over all space in terms of the solid angle. As there are exactly  $4\pi$  steradians in a circle, we obtain:

$$\sigma_s = \int b^2 d\Omega = 4\pi b^2 \quad (2.30)$$

From which it follows that the scattering cross section forms a with a radius equal to the scattering length. In a sense, the scattering cross section describes the size of the nucleus as seen by the neutron, where the scattering length is the effective radius of the nucleus in this case. Note how the scattering length varies unsystematically across the periodic table and is not a single function of the mass number of the element.

### 2.2.1 Origin of neutron scattering lengths [15]

The neutron scattering length is often considered to vary randomly for each isotope. It is however possible to make a rough estimation of the neutron

scattering length. We consider a neutron with an energy  $E_i$  being scattered from an attractive square well potential at  $-V_0$ . The well has a width of  $2R$ , and a potential of  $V_0 \gg E_i$ . Starting from the Schrödinger equation we've got:

$$\left( \frac{\hbar^2}{2m} \nabla^2 + V(r) \right) \Psi(r) = E \Psi(r) \quad (2.31)$$

Outside of the square well, the potential  $V(r) = 0$ , and so the solution to the equation becomes:

$$\Psi_{s,out} = \frac{\sin kr}{kr} - b \frac{e^{ikr}}{r} \quad (2.32)$$

where  $k = \sqrt{2mE_i}\hbar$ . Inside the square well, the solution becomes:

$$\Psi_{s,in} = A \frac{\sin qr}{qr} \quad (2.33)$$

where the wave number  $q$  is described as  $q = \sqrt{2m(E_i + V_0)}\hbar$ . Note that the factor  $kr \ll 1$  due to the very small neutron mass and we can therefore approximate equation 2.32 as:

$$\Psi_{s,out} \approx 1 - \frac{b}{r} \quad (2.34)$$

Since the wave function has to be completely continuous over all space, we can use the boundary condition  $|r| = R$  to get:

$$\Psi_{s,out} = \Psi_{s,in} \quad (2.35)$$

at the boundary, which leads to:

$$1 - \frac{b}{R} = A \frac{\sin qR}{qR} \quad (2.36)$$

which can be rewritten to:

$$R - b = A \frac{\sin qR}{q}. \quad (2.37)$$

Even at the derivative, these functions need to be continuous, which gives us:

$$\frac{d}{dR}(R - b) = \frac{d}{dR} A \frac{\sin qR}{q}. \quad (2.38)$$

$$1 = A \cos qR \quad (2.39)$$

## 2. Scattering Theory

---

$$A = \frac{1}{\cos qR} \quad (2.40)$$

Combining equation 2.37 and 2.40 gives us:

$$R - b = \frac{1}{\cos qR} \frac{\sin qR}{q}, \quad (2.41)$$

Rewriting the sine and cosine into a tangent:

$$R - b = \frac{\tan qR}{q}, \quad (2.42)$$

And finally, we can express the ratio  $b/R$  as a function of  $qR$ :

$$\frac{b}{R} = 1 - \frac{\tan(qR)}{qR} \quad (2.43)$$

This equation gives a first order estimate of the scattering length  $b$ . As can be seen in figure 2.2,  $b/R$  varies extremely sharply as a function of  $qR$ , which means that the scattering length can jump to a completely different value for each added nucleus. This is illustrated further by the highlight of hydrogen-1 (H) and deuterium (D) which have a large contrast in scattering length despite belonging to the same element. It can also be seen that the scattering length can be negative for certain isotopes, this corresponds to a negative phase shift upon scattering.

Note that this is merely an approximation, apart from the mathematical simplifications we have ignored both absorption and the magnetic component of the neutron scattering length. The imaginary part of the scattering length, which describes the absorption, is generally very low for neutrons which is in many cases a reason to opt for neutrons over X-rays as this allows the penetration of much larger samples. The magnetic component of the scattering length can be used with polarised neutron reflectivity in order to investigate magnetic properties of a material.

### 2.2.2 Scattering length density

While the total scattering power of a single nucleus can be well described in terms of scattering length, in order to get a good measure of the total scattering power of a material we also need to take the physical density into account. If the nuclei are more tightly packed, there will be more nuclei per unit volume to scatter from, which inevitably leads to stronger scattering. The total scattering power of a material is therefore described in terms of

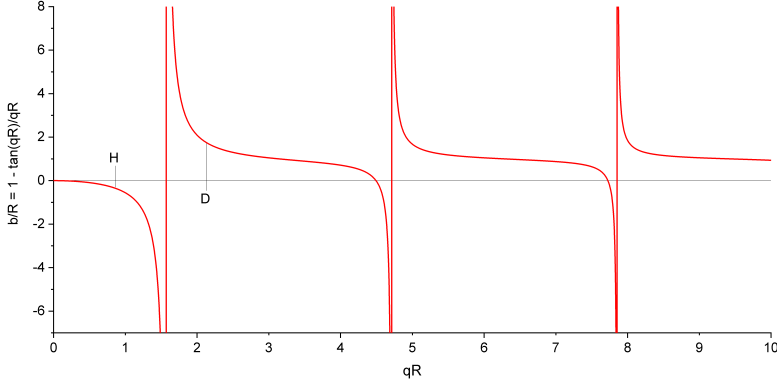


Figure 2.2: The ratio  $b/R$  varies very sharply as a function of  $qR$ , meaning the scattering length  $b$  can move to a seemingly random value for each added nucleus.

scattering length density (SLD), which can be calculated by summing the scattering lengths of each element in the material and dividing this by the volume of the unit cell [9]:

$$\text{SLD} = \frac{\sum_{i=1}^N b_i}{V_m} \quad (2.44)$$

Where  $b_i$  is the scattering length of each element and  $V_m$  is the volume of the unit cell. Note how this does not need to be an actual unit cell as seen in crystallography, it is indeed a representative volume of the material which in principle can be completely amorphous. As an amorphous material does not have a well defined crystal to define a volume, it can be calculated using the bulk density of the unit cell and the molecular weight:

$$V_m = \frac{M}{\rho N_a} \quad (2.45)$$

Where  $\rho$  is the density of the material,  $N_a$  is the Avogadro constant. The scattering density of a composite material can then be calculated by putting equation 2.45 into equation 2.44:

$$\text{SLD} = \frac{\rho N_a \sum_{i=1}^N b_i}{\sum_{i=1}^N b_i M_i} \quad (2.46)$$

## 2. Scattering Theory

---

The scattering density relates directly to the refractive index of neutrons as provided in equation 2.11, rewritten here for clarity:

$$n = 1 - \frac{\lambda^2}{2\pi} \cdot \text{SLD} \quad (2.47)$$

Because of this linear relationship between SLD and refractive index, the SLD is often considered to be a direct analog to the refractive index.

### 2.3 Choice of materials

The materials that are being used in neutron multilayers are primarily based on the SLD of these materials. The imaginary component of the SLD needs to be as low as possible for both materials as this component describes absorption. Meanwhile, for the real component we need a high contrast in SLD, as this equates to a large contrast in scattering potential as described in chapter ABOVE. To illustrate, the real and imaginary parts of a set of materials are plotted in figure 2.3. As this is a prerequisite, we only look at materials with low imaginary SLD here (several orders of magnitude lower than the real part). Now we simply need to pick two materials that have a large difference in the real part of the SLD. Beryllium may seem like a reasonable candidate on paper, but since it undergoes nuclear reactions upon neutron irradiation, nickel is a better material for neutron multilayers. Therefore the combination of nickel and titanium is the usual option, as highlighted figure. Note that some materials with intermediate values are emitted in order to increase readability.

### 2.4 Neutron scattering in reciprocal space

It can be extremely convenient in neutron scattering to describe phenomena in reciprocal space instead of real space. This convenience arises from the fact that the diffraction pattern is directly related to the reciprocal space of the SLD-profile of the material, so by becoming familiar with this description, one can tell a lot about the structural properties of a given multilayer simply from a glance at the obtained diffraction pattern [16]. The reciprocal space corresponds to the Fourier transform of real space, and is often also called q-space or Fourier space.

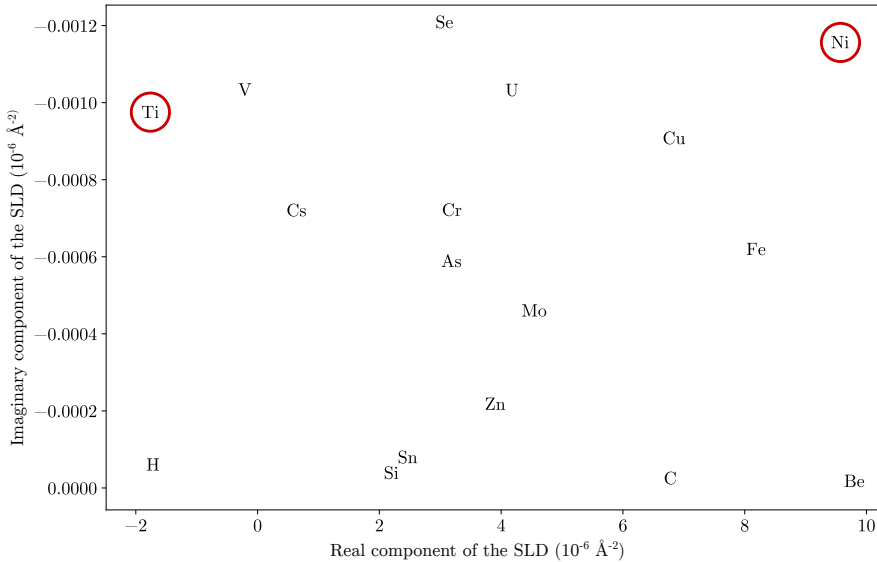


Figure 2.3: A selection of materials with their scattering lengths are plotted for low imaginary values, a system with Ni/Ti offers a large contrast in the real SLD with low values for the imaginary part.

### 2.4.1 Reciprocal space

To understand the diffraction pattern in reciprocal space we imagine an incoming neutron wave that scatters upon an interface as shown in figure 2.4a. The incident and scattered wave vector are denoted by  $\mathbf{k}_i$  and  $\mathbf{k}_f$  respectively. The scattering vector is described by the vector  $\mathbf{q}$  and can be expressed as  $\mathbf{q} = \mathbf{k}_f - \mathbf{k}_i$  [17]. From geometry, we can see that:

$$\sin \frac{2\theta}{2} = \frac{0.5\mathbf{q}}{\mathbf{k}_i} \quad (2.48)$$

Where we can use  $\mathbf{k}_i = 2\pi/\lambda$  to show:

$$q = \frac{4\pi}{\lambda} \sin \theta \quad (2.49)$$

Which is the equation that is generally used to convert from q-space to  $\theta$ . The points in q-space where diffraction peaks are found can be illustrated using an Ewald sphere construction, as shown in figure 2.4b. The incoming

## 2. Scattering Theory

---

wave vector  $\mathbf{k}_i$  is drawn with its tip drawn at the scattering site. A sphere is drawn around this vector, and a diffracted beam will be formed if the drawn sphere intersects with an interface in reciprocal space. From this, we can see how a diffraction peak can be observed at the given incidence angle  $2\theta$ , corresponding to the third peak in q-space. We can also note how the diffraction peaks are equidistant to each other with a distance of  $2\pi/\lambda$ . During a specular neutron reflectivity experiment, a scan is made in the  $\mathbf{q}_z$  direction by varying the incidence angle  $\theta$ .

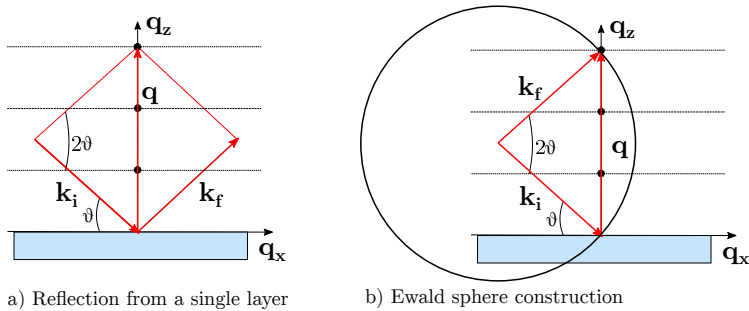


Figure 2.4: a) An incoming neutron wave with incident and refracted wave vector  $\mathbf{k}_i$  and  $\mathbf{k}_f$  scatters upon an interface. The scattering vector  $\mathbf{q}$  is obtained by  $\mathbf{q} = \mathbf{k}_f - \mathbf{k}_i$  and is in the  $\mathbf{q}_z$  direction for specular scattering. b) The Ewald sphere construction can be used to illustrate for which incidence angles a diffraction peak can be found

### 2.4.2 Fourier expansion for an ideal multilayer

The intensity profile that is obtained by experiment is directly dependent of the SLD-profile in the probed direction, as explained in subchapter 2.1. For a perfect multilayer with abrupt interfaces, the SLD-profile in the depth direction will have the form of a square wave. The obtained intensity profile can then be explained by the Fourier transform of this profile. The SLD-profile can be written as an infinite series of cosines and sines [17]:

$$g(z) = a_0 + \sum_{n=1}^{\infty} \left[ a_n \cos\left(\frac{2\pi}{\Lambda} nz\right) + b_n \sin\left(\frac{2\pi}{\Lambda} nz\right) \right] \quad (2.50)$$

As an example, we take such an SLD profile for a multilayer with two distinct layers having a thickness of 1 nm each without any interface imperfections. The amplitude of the SLD is chosen to be equal to  $1 \text{ \AA}^{-2}$ , as can be seen by the square wave in figure 2.5. The first term  $a_0$  can be easily found by evaluating the SLD-function over one period. The resulting integral can be found using easy geometry, as the integral simply equals the total area under the curve. For the first period, the total area evidently equals zero:

$$a_0 = \int_0^{\Lambda} g(z) dz = 0 \quad (2.51)$$

The terms for  $a_n$  can be found in a similar way:

$$a_n = \frac{1}{0.5\Lambda} \int_0^{\Lambda} g(z) \cos\left(\frac{2\pi}{\Lambda} nz\right) \quad (2.52)$$

$$= \frac{2}{\Lambda} \int_0^{0.5\Lambda} \cos\left(\frac{2\pi}{\Lambda} nz\right) - \frac{2}{\Lambda} \int_{0.5\Lambda}^{\Lambda} \cos\left(\frac{2\pi}{\Lambda} nz\right) \quad (2.53)$$

$$= \frac{4}{\Lambda} \int_0^{0.5\Lambda} \cos\left(\frac{2\pi}{\Lambda} nz\right) = 0 \quad (2.54)$$

Note how all even Fourier components dissapear, this is a direct result from the fact that both layers in the multilayer have an equal thickness. The ratio between the thicknesses of the individual layers in the bilayer is an important parameter and is usually denoted as  $\Gamma = l_a/l_b$  where  $l_a$  and  $l_b$  denote the thickness of each layer in the bilayer. In general it follows from the Fourier composition that for a  $\Gamma$ -value of  $1/m$ , every  $m$ 'th component will dissapear. In this example where the layers are equally thick we get  $\Gamma = 0.5$ , meaning every second component will dissapear. This leaves us with a series of sines:

$$g(z) = \sum_{n=1}^{\infty} b_n \sin\left(\frac{2\pi}{\Lambda} nz\right) \quad (2.55)$$

## 2. Scattering Theory

---

Evaluating the sine gives us:

$$b_n = \frac{1}{0.5\Lambda} \int_0^{\Lambda} g(z) \sin\left(\frac{2\pi}{\Lambda} nz\right) \quad (2.56)$$

$$= \frac{2}{\Lambda} \int_0^{0.5\Lambda} \sin\left(\frac{2\pi}{\Lambda} nz\right) - \frac{2}{\Lambda} \int_{0.5\Lambda}^{\Lambda} \sin\left(\frac{2\pi}{\Lambda} nz\right) \quad (2.57)$$

$$= \frac{4}{\Lambda} \int_0^{0.5\Lambda} \sin\left(\frac{2\pi}{\Lambda} nz\right) \quad (2.58)$$

$$= \frac{2}{n\pi} (1 - \cos n\pi) \quad (2.59)$$

Which can be reduced to:

$$b_n = \begin{cases} 0, & \text{if } n \text{ is even.} \\ \frac{4}{n\pi}, & \text{if } n \text{ is odd.} \end{cases} \quad (2.60)$$

This leaves us with our final Fourier series for a square wave:

$$g(z) = \sum_{n=1}^{\infty} \frac{4}{n\pi} \sin\left(\frac{2\pi}{\Lambda} nz\right) \quad (2.61)$$

This result is illustrated in figure 2.5. The square wave illustrates the actual SLD-profile, while the sinusoidal waves are the Fourier components as described in equation 2.61, in this illustration only the first three components are shown. The amplitudes of the peaks of the measured signal in a scattering experiment are directly proportional to the amplitudes of the Fourier components described here. This makes it clear how a higher contrast in scattering potential results in a stronger signal. A similar analysis is valid for interfaces with interface imperfections, where the transition from one layer to another is more gradual. While the resulting Fourier components will be different from equation 2.61, it can be seen from the described example in figure 2.5 that the first component of the Fourier series is very sensitive to the contrast in SLD between the layers, while the other components will be more sensitive to the interface width.

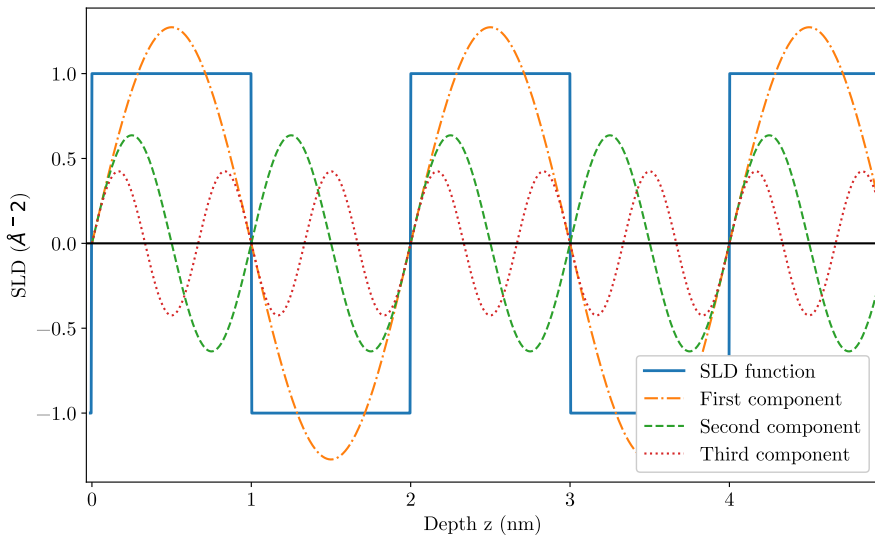


Figure 2.5: The interface width can be described as an infinite series of a sine waves. The first three components of the Fourier series are shown in this figure, summing all Fourier components will eventually result in the sketched square wave.



# Chapter 3

## Multilayer and supermirror optics

### 3.1 Reflectivity from different interfaces

To get to the reflectivity for multilayer instruments, we will start with the simplest case of reflectivity from a substrate. After that, we will expand this to the case of a single layer on top of a substrate, followed by a multilayer.

#### 3.1.1 Substrate

Reflectivity on a single substrate describes the simplest form of Fresnel reflectivity, which is covered in subsection 2.1.1. The measured intensity can then be expressed using the fraction of reflected intensity as given in equation 2.19, and multiplying it with the incident intensity  $I_0$ :

$$I = I_0 \left[ \frac{q - \sqrt{q^2 - q_c^2}}{q + \sqrt{q^2 - q_c^2}} \right]^2 \quad (3.1)$$

A simulated intensity profile resulting from this expression is shown in figure 3.1, where an incident neutron beam with a wavelength of 5.0 Å reflects upon a silicon substrate.

#### 3.1.2 Single layer

Now if we add a single layer to the substrate, we will also have reflections from the finite thickness of this layer. The resulting reflection can most clearly be understood by tracing an incoming beam, as shown in figure 3.2. The incoming beam partly reflects at the surface, while another part gets transmitted through the top layer and reflected at the substrate interface. The phase difference between the two transmitted beams depend on the optical path, and it follows from the figure that this can be described by:

$$\Delta = (AB + BC)n - AD \quad (3.2)$$

### 3. Multilayer and supermirror optics

---

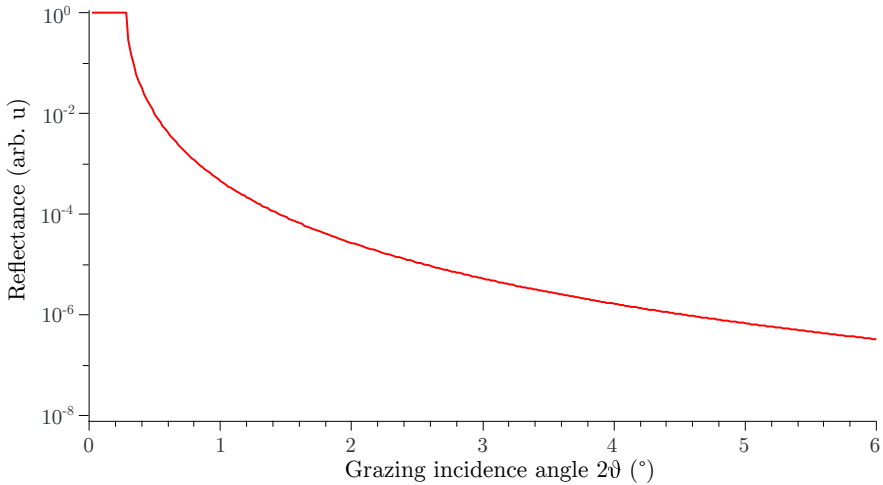


Figure 3.1: A simulation of the reflectance for a single layer of nickel with a thickness of 30 nm on a Si substrate and a Neutron wavelength of 5 Å.

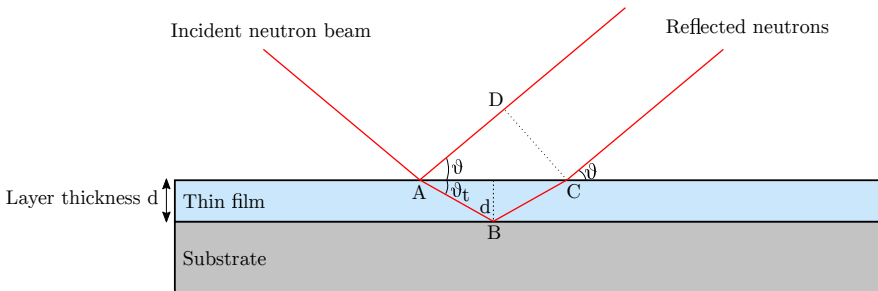


Figure 3.2: An incoming neutron beam hits a single thin film from the substrate.

Where  $n$  is the refractive index of the layer. From simple geometry in the figure, it also follows that the path difference can be described as:

$$\Delta = 2d \sin(\theta_t) \approx 2d\sqrt{\theta^2 - \theta_c^2} \quad (3.3)$$

From the left-hand side, we can see that this is analogue to the Bragg equation, where a maximum occurs whenever the phase difference is a multiple of the

wavelength, or when  $\Delta = m\lambda$ . Filling this into the right-hand side, we can re-write this as [18]:

$$\theta_m^2 = \theta_c^2 + \left( \frac{\lambda}{2d} \right) m^2 \quad (3.4)$$

Such a reflection is simulated in figure 3.3. Where a neutron-beam is reflected from a single layer of nickel with a thickness of 30 nm. It follows from equation

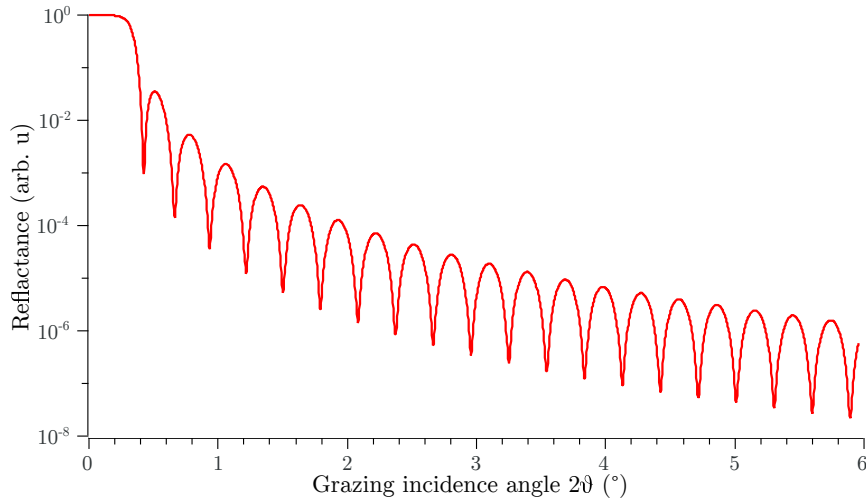


Figure 3.3: A simulation of the reflectance for a single layer of nickel with a thickness of 30 nm on a Si substrate and a Neutron wavelength of 5 Å.

3.4, that the spacing between these maxima that can be observed are inversely dependent on the thickness of the layer. Meaning that a thicker layer leads to a closer spacing between the fringes while a very thin layer will see these fringes very far apart.

### 3.1.3 Multilayers

We can expand this concept as well to multilayers. The multilayers in this work consist of a certain number of so-called bilayers, which is a repeated set of two layers that get repeated throughout the stack. A schematic drawing of such a multilayer is seen in figure 3.4 As can be observed in figure, the

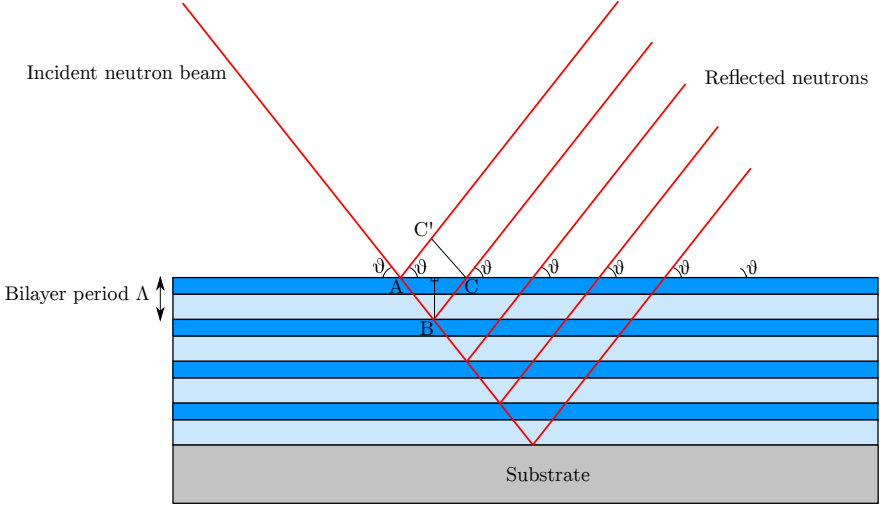


Figure 3.4: A schematic overview showing reflection from a multilayer. For pedagogical purposes, only one reflected beam is drawn per bilayer. In reality, reflection occurs for every layer in the bilayer.

difference in optical path between the reflected beams depends on the total thickness of one bilayer. The total thickness of one bilayer is known as the period, and is denoted with  $\Lambda$ . The position of the fringes that arise from the periodicities can be described in a similar way as equation 3.4, but where we use the bilayer thickness instead of the individual layer thickness:

$$\theta_m^2 = \theta_c^2 + \left( \frac{\lambda}{2\Lambda} \right) m^2 \quad (3.5)$$

Apart from these maxima, which are known as Bragg peaks, can we also describe so-called Kiessig fringes between the peaks. These fringes arise from the total thickness of the multilayer. Assuming there is no damping due to roughness for example, we can observe  $N - 2$  of these Kiessig fringes between

the maxima from the layer periodicity [18]. This is also shown in figure 3.5, where clear Kiessig are observed between the larger Bragg peaks.

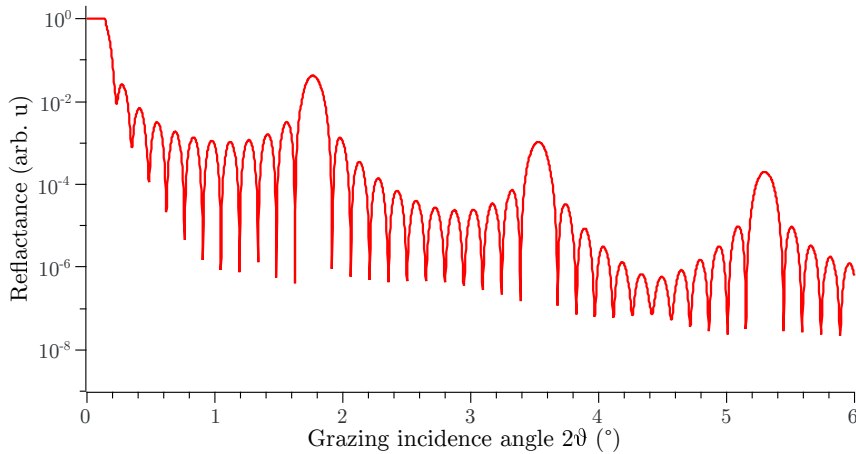


Figure 3.5: A simulation of the reflectance for a multilayer system consisting of 12 bilayers of Ni and Ti, with a total period of 50 nm.

### 3.2 Interface imperfections

So far, we have assumed reflection from ideal interfaces. In reality however, interfaces are not perfectly flat or abrupt. Meaning the interfaces have a certain thickness in the normal direction, this thickness is called the interface width and is denoted by  $\sigma$ . In reality, the interface width arises from two different physical factors. The abruptness of the interface, which arise from factors such as interdiffusion and intermixing, and the interfacial roughness. These two physical factors behave independently, a perfectly flat sample can still contain intermixing while a rough sample still can be perfectly abrupt on a local level. The total interface width can therefore be considered as the sum of these effects, and can thus be expressed as:

$$\sigma^2 = \sigma_d^2 + \sigma_r^2 \quad (3.6)$$

Where  $\sigma_d$  describes the interface width due to the intermixing and interdiffusion and  $\sigma_r$  describes the interface width due to the roughness. Note how the exact deviation from a perfect interface varies on a local level, the interface width is therefore defined as a square root averaged value over the probed interface. If we consider the SLD-profile of such imperfect interfaces, it follows that the effects of intermixing and interfacial roughness are indistinguishable from each other in the normal direction. Both factors lead to a more gradual transition of SLD from one interface to the other. This loss of an abrupt transition leads to a reduction of specular reflectivity. In the case of interfacial roughness, part of the incident beam will be scattered into non-specular directions while intermixing leads to an increase in transmission. These different causes of interface width can therefore be observed by doing non-specular scans, but in specular reflectivity these effects are indistinguishable from each other, as is illustrated in figure 3.6. A typical distribution of the interface profile in the normal direction is

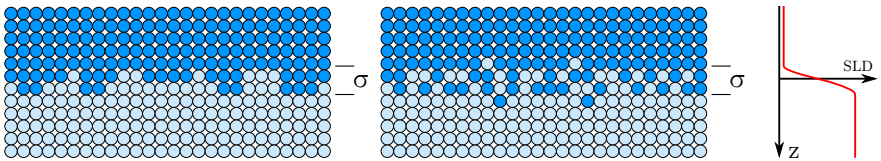


Figure 3.6: While intermixing and surface roughness are distinct phenomena, they are indistinguishable in the SLD profile normal to the interface.

given by the error function:

$$g(z) = \operatorname{erf}\left(\frac{z}{\sqrt{2}\sigma}\right). \quad (3.7)$$

The derivative of the error function shows how the profile depends on the probed z-direction, this turns out to be a Gaussian distribution [19]:

$$f(z) = \frac{dg}{dz} = \frac{1}{\sqrt{2\pi}\sigma^2} e^{-\frac{1}{2}\left(\frac{z}{\sigma}\right)^2} \quad (3.8)$$

The attenuation factor in the diffraction pattern follows from the Fourier transform, this is another Gaussian function. So the attenuation factor associated with our Fresnel equations can be described as

$$\tilde{f}(z) = e^{-\frac{s^2\sigma^2}{2}\left(\frac{4\pi\sigma\sin\theta}{\lambda}\right)^2} \quad (3.9)$$

This factor is known as the Debye-Waller factor and is commonly used to simulate imperfect interfaces [20]. From this factor and combining it with Fresnel equations, we find that the reflectivity of a multilayer can be described as:

$$R = R_0 e^{-(2\pi m \frac{\sigma}{\lambda})} \quad (3.10)$$

Note that the reflectivity of a sample depends exponentially squared on the interface width. So even a modest improvement of the interface width has a large impact on the total reflectivity. The influence of the multilayer period can be explained by the fact that a multilayer with a smaller period has a larger fraction of the layer consisting of interfaces. The smaller the period, the more important the quality of the interface therefore becomes for a good reflectivity performance.

### 3.3 Off-specular scattering

So far we have only considered the specular part of the reflection, where the angle of incidence is equal to the angle of refraction. For an ideal interface, the scattering potential in the in-plane direction is always constant, meaning all scattering will be in the specular direction normal to the plane of incidence. In the case of surface roughness however, local differences occur in the chemical composition of sample in the in-plane direction. This means that the parallel components of the neutron beam experience a potential barrier, leading to partial reflection in the in-plane direction. This phenomenon, where scattering occurs outside of the specular direction is named off-specular

### 3. Multilayer and supermirror optics

---

scattering. This is further illustrated in figure 3.7, where an incoming neutron beam reflects from the sample and reaches the detector, the specular signal can be found in the plane of incidence while the off-specular signal is perpendicular to the plane of incidence. Since off-specular scattering probes the in-plane direction of the interface, one can obtain a lot of information of the roughness profile of the interfaces. Interfacial roughness for example leads strong scattering potential barriers in the off-specular direction, and therefore increases the off-specular signal. Intermixing however leads to a much more gradual contrasts in the in-plane direction and contributes therefore much less to the off-specular signal. There are several parameters

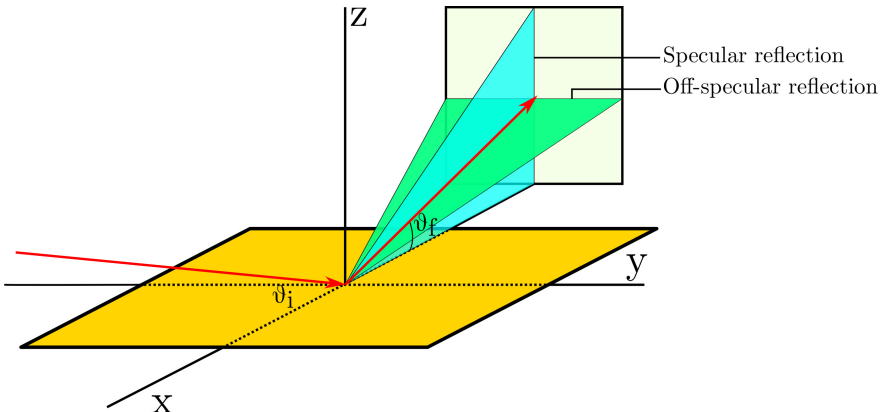


Figure 3.7: An incoming neutron beam reflects from the sample and reaches the detector, the specular signal can be found in the plane of incidence while the off-specular signal is perpendicular to the plane of incidence.

that influence the off-specular signal in a multilayer. The most important ones that we will describe here are the cross correlation length, the transverse correlation length and the Hurst parameter. The cross correlation length of a multilayer describes how closely correlated the roughness profile is between the subsequent interfaces within the multilayer. This parameter is particularly interesting for this work, as correlated roughness means that deviations from an ideal layer at the interface repeat themselves for subsequent layers, meaning that such deviations may increase with each newly deposited layer. This phenomenon, which is called accumulated roughness, is a particular challenge when depositing multilayers with many periods as is conventional with neutron supermirrors for example. Correlated roughness

in a multilayer can be detected in the off-specular signal by looking at the so-called Bragg sheets. When the interface profile is completely uncorrelated, the off-specular signal scatters into different directions for each layer within the sample, meaning the off-specular signal will be spread out over the entire reciprocal plane. For completely correlated layers, the off-specular signal is scattered into the same direction for each layer. As the periodicity of this interface profile is the same as the multilayer period, this signal will be focused on in perpendicular sheets around the Bragg peaks of the specular signal. This is illustrated in figure 3.8 The lateral correlation length is sometimes described as the cut-off for the length scale where an interface begins to look smooth. The absolute magnitude of the interface width can very well be low, but the interface still looks very rough if the lateral correlation length is low enough. This is illustrated in figure 3.9, the lateral correlation length basically describes the typical distance between the peaks in this figure. Finally the Hurst parameter describes the jaggedness of the interfaces in the sample. A sample with a Hurst parameter of 1.0 looks relatively smooth where the interfaces gets more jagged the closer the Hurst parameters gets to zero. This parameters influences the the shape of the off-specular signal. A more ideal sample with low jagged shows a more Gaussian distribution in the off-specular reflectivity, where this shape becomes very Lorentzian for very jagged samples.

### 3. Multilayer and supermirror optics

---

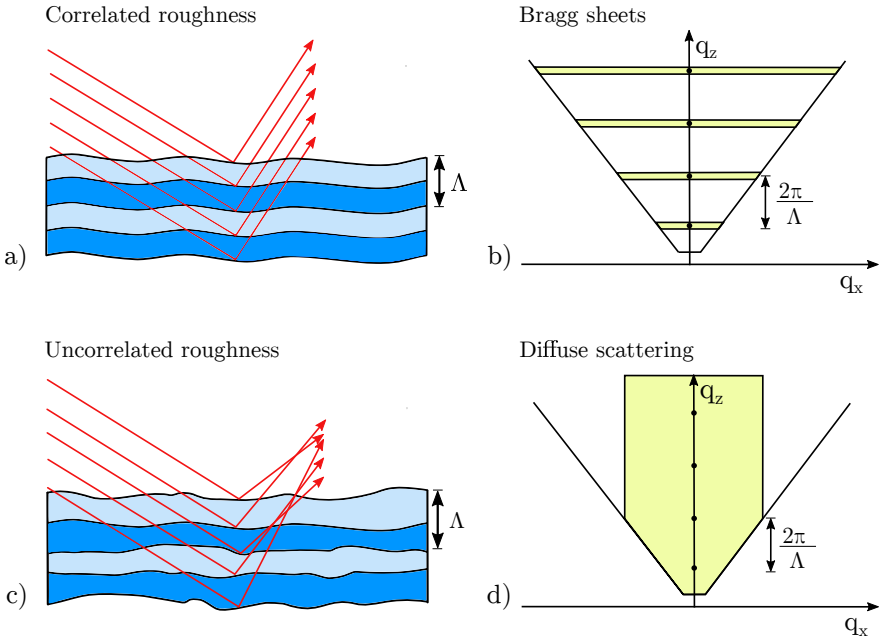


Figure 3.8: a) Reflection for very correlated layers. As the interface imperfections are similar for each layer, scattering will occur in the same direction for each layer. b) The off-specular mapping for neutron reflection with correlated roughness. As the rays are scattered in the same direction, very concentrated Bragg sheets arise around the same  $q_z$  values whenever the specular Bragg condition is fulfilled. c) Reflection for uncorrelated layers. As the interface imperfections are different for each layer, the resulting scattering direction will be different as well. d) The off-specular mapping for neutron reflection with uncorrelated roughness. The uncorrelated layers give rise to a spread-out diffuse signal over  $q$ -space.

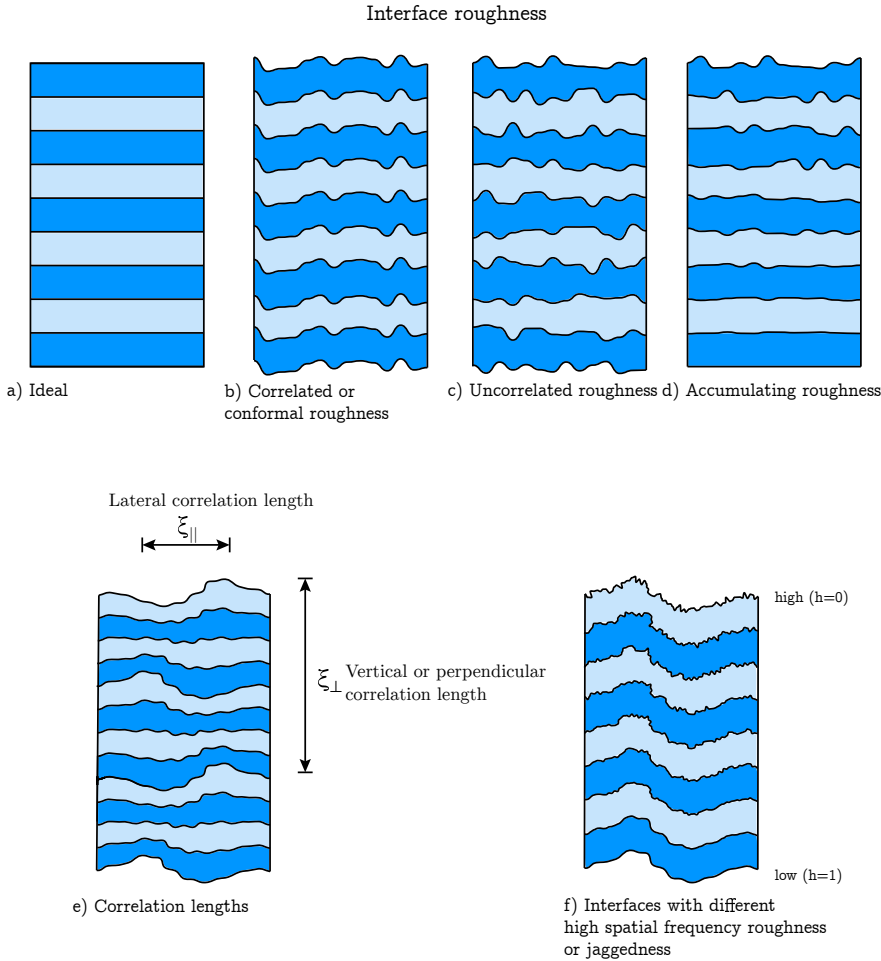


Figure 3.9: a) An ideal multilayer with flat and abrupt interfaces. b) Correlated roughness, the roughness profile for each interface is repeated throughout the layer. c) Uncorrelated roughness, the roughness profile is independent for each layer. d) Accumulating roughness, the interface width increases throughout the multilayer. e) The lateral correlation length and the vertical correlation length scale for a multilayer. f) Interfaces with increasing jaggedness throughout the multilayer. Note how a low Hurts parameter corresponds to a more jagged layer with high spatial frequency.



# Chapter 4

## Multilayer Depositions

In order to create high quality multilayers a proper understanding of the growth technique is necessary. In this chapter we will explain the techniques used to grow the samples discussed in this work, starting by an introduction on magnetron sputter deposition itself.

### 4.1 Magnetron sputter deposition

One of the most popular techniques to grow multilayers is physical vapor deposition (PVD) [21]. Magnetron sputter deposition is a common type of PVD, which is used to grow the samples in this work. The basic working principle behind sputtering is intuitively quite simple. A steady flow of noble gas is led into a vacuum chamber. Meanwhile, a bias is applied to the sputtering target, which contains the material that will be deposited upon the substrate. Stray electrons near the target are accelerated towards the substrate due to the electric field that is present, colliding with neutral atoms from inlet sputtering gas on the way. If these electrons have gained sufficient energy upon collision, it may knock off an electron from the sputtering gas, converting it in to a positively charged ion [22]:



Note how two additional electrons are released during this ionization process, these too are accelerated by the electric field and can bombard additional gas atoms generating even more free electrons. Meanwhile the ionized atoms, which are positively charged, will be attracted to the negatively charged sputtering target. Upon collision, both target atoms as well as secondary electrons are ejected. The secondary electrons will be accelerated and ionize even more neutral gas atoms while part the ejected target atoms will land on the substrate surface, slowly creating a uniform layer of the target material. This state of ionized gas is known as a plasma, and is generally considered as an own state of matter. Upon the electron excitation of the sputtering gas, photons will be emitted which gives the visible plasma a visible glow. In order for the plasma to be sustained, there has to be a sufficient amount of collisions between electrons and sputtering atoms. The secondary electrons are therefore important to sustain the plasma [22].

#### 4. Multilayer Depositions

---

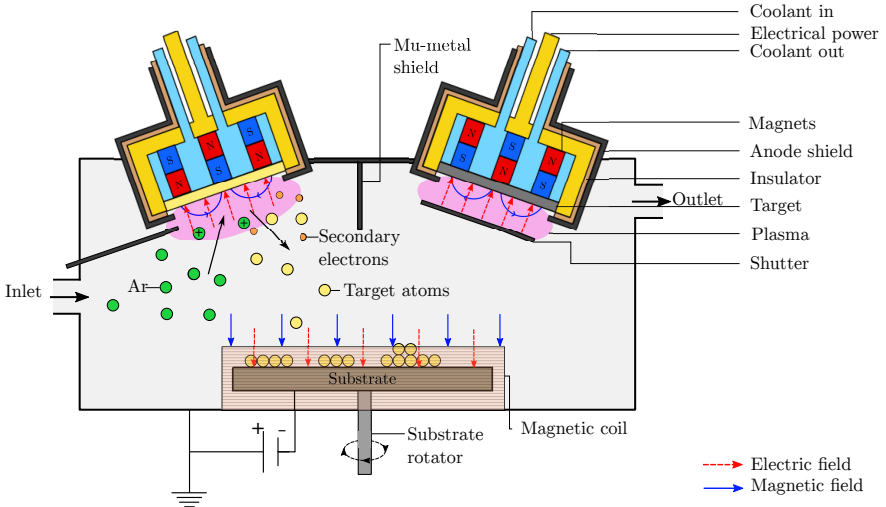


Figure 4.1: A simplified sketch of magnetron sputtering. Incoming Argon ions collide upon the sputtering target, knocking out target atoms which in their turn form a new layer of the material on the substrate.

In order to maximize the amount of secondary electrons that can be used for the ionization process magnets are placed behind the target material. The subsequent Lorentz force on the electron provides a path for the electrons to follow. A typical orientation of these magnets can be seen in figure 4.1, where the magnetic field is orientated radially above the target surface. The resulting path will follow a direction according to the cross-product  $\mathbf{E} \times \mathbf{B}$ , forming a circular trajectory above the target surface. Given the preferential status of this path for the electrons, the ionization rate will be higher in this region leading to a higher plasma density. It is for this reason that a circular erosion zone appears on used targets [23].

## 4.2 Ion Assistance

In order to optimize the growth process and create smooth and abrupt layers, it is important to consider the energy of the incoming adatoms on the multilayer that is being deposited. When the adatom energy is too low, the surface mobility will be very limited meaning incoming adatoms will stick directly to their landing sites. Because of this, any deviation in the film surface will not be evened out but instead will be repeated. Such growth will therefore lead to rough surfaces with a lot of accumulated roughness [19].

Increasing the adatom energy will increase the surface mobility, adatoms that land on the surface can migrate to another spot, smoothening out the deposited layer. It is therefore important for a smooth film, to increase the adatom mobility. One way to do this, is to use the ions that are available in the plasma during film growth [24]. By applying a negative bias on the substrate, there will be a significant potential drop towards the substrate meaning the ions will be accelerated towards the film. By controlling the bias on the substrate, the ion-atom ratio can be controlled such that there is enough energy per adatom to enable surface migration at the landing sites. These different cases of film growth are illustrated in figure 4.2.

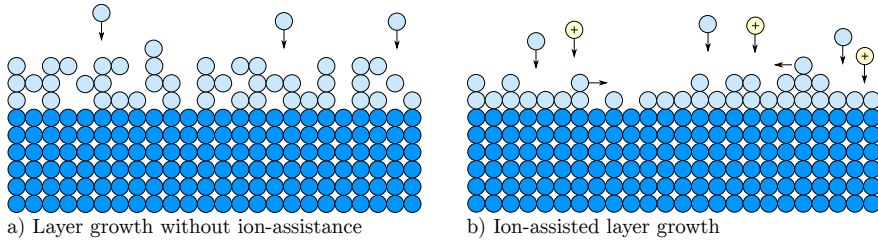


Figure 4.2: a) Film growth with low adatom energy, adatoms stick directly to their landing sites leading to a rough surface. b) Ion-assistance during layer growth increases adatom mobility, making surface migration possible. Note how the ions are not part of deposited layer, instead they recoil in the form of neutral gas atoms [25].

However, the high-energy bombardments of ions can lead to intermixing at the interfaces, meaning particles of the film will be displaced into the substrate. Using a too high energy therefore leads to an increase in intermixing, which essentially has the same effect as regular roughness. It is therefore important to find a good balance between the smoothening effect due to surface migration at high adatom energies, and the lack of intermixing that comes

#### 4. Multilayer Depositions

---

with low adatom energies. The plasma can be guided using a magnetic field near the substrate, such that a lower ion energy is required for surface migration, there will however still remain intermixing between the two layers.

While this intermixing effect is mainly limited to the first atomic layer, the multilayers in this work have an interface width that is roughly in the order of the atomic spacing. Such small displacements can therefore lead to a significant increase in the total interface width and should therefore be avoided.

In order to achieve this, a so called split-bias scheme is used during the growth of the deposited multilayers. In this set-up, an initial layer is grown with a low bias at the substrate. This layer initial layer is therefore grown with a very low adatom energy, leading to relative rough growth at a lower density, but without any intermixing. After an initial part of the layer is grown using this low-bias scheme, the bias is increased in order to allow for surface migration when the adatom reaches the surface, smoothening the rest of the layer. While there will be intermixing at this higher bias, the intermixing will be limited to the initially grown layer which is the same material. The initially grown layer therefore acts as a buffer layer, to protect the lower layer against intermixing. This process with an alternating bias scheme is repeated throughout the deposition of the entire multilayer, leading to smooth and abrupt surfaces [19]. This scheme is illustrated in figure 4.3

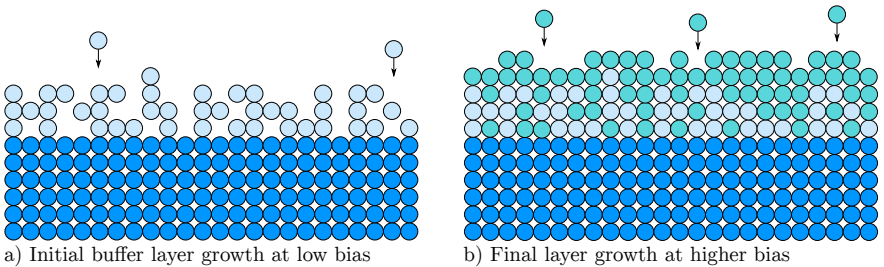


Figure 4.3: a) An initial buffer layer is grown with a low substrate bias. This leads to a very rough initial layer without intermixing. b) The rest of the layer is grown with a higher substrate bias, giving the adatoms enough energy to migrate. the buffer layer prevents intermixing into the layer beneath. The different colours for the initial and final layers are for the purpose of clarity, they are the same material.

### 4.3 $^{11}\text{B}_4\text{C}$ co-deposition

When growing multilayers using magnetron sputtering, nanocrystallites tend to form throughout the sample. These crystallites lead to faceted interfaces between the layers which can contribute to an increased interface width. Another contributing factor to the interface width is the formation of intermetallics between the layers, decreasing the abruptness between the layers. Furthermore, roughness patterns at the interface tend to be replicated leading to roughness accumulation. It would therefore be beneficial to eliminate the formation of crystallites by growing an amorphous multilayer instead. This can be established by co-depositing  $^{11}\text{B}_4\text{C}$  during the growth process. The addition of boron to the layer inhibits the formation of crystallites, leading to amorphous layers throughout the entire multilayer. Using a continuous deposition of  $^{11}\text{B}_4\text{C}$  during the growth process, boron is added through the entire multilayer. For neutron multilayers it is important to consider that the the boron-10 isotope, which is present in natural boron, absorbs neutrons. The boron-11 isotope however is transparent to neutrons, it is for this reason that an isotope enriched  $^{11}\text{B}_4\text{C}$  target is used during the deposition. The power to the  $^{11}\text{B}_4\text{C}$  magnetron is constant during the entire deposition, resulting in a stable  $^{11}\text{B}_4\text{C}$ -flux during film growth. Note that the addition of  $^{11}\text{B}_4\text{C}$  leads to a dilution of the SLD-contrast between the interfaces, adding too much  $^{11}\text{B}_4\text{C}$  therefore leads to a reduction in reflectivity. The power that is used for the  $^{11}\text{B}_4\text{C}$ -target is therefore tweaked such that it is high enough to make the entire sample is amorphous, but not increased any further to prevent unnecessary dilution in SLD-contrast between the interfaces.

### 4.4 Reducing interface width

When designing high-performance neutron multilayers, it is essential to consider the interface width in the sample. A combination of the techniques above is used to minimize the total interface width as much as possible. The co-deposition of  $^{11}\text{B}_4\text{C}$  removes all crystallinity of the multilayer. However, the adatom mobility during deposition is also significantly reduced leading to a strong accumulation of interface width throughout the layer. A high ion-assistance is therefore needed to increase the adatom mobility enough to allow for surface diffusion. These adatom energies however lead to a strong intermixing between the interfaces, making it essential to combine the  $^{11}\text{B}_4\text{C}$  co-deposition with the split-bias ion-assistance technique. The resulting deposition scheme therefore incorporates the split-bias scheme as

described in chapter 4.2. Where an initial buffer layer is grown with a low bias, followed by the rest of the layer grown with a higher substrate bias. During this entire process,  $^{11}\text{B}_4\text{C}$  is co-deposited throughout the multilayer to inhibit the formation of crystallites. The bias used during the process needs to be fine-tuned, such that intermixing does not exceed the initial buffer layer, while being high enough to allow for surface diffusion.

## 4.5 Deposition system at PETRA III

The samples that are described in this thesis have been deposited at a ultra-high vacuum (UHV) magnetron sputtering chamber at PETRA III at the Deutsches Elektronen-Synchrotron in Hamburg, Germany [26]. The system is mounted on a 1-tonne ultra-high load, high resolution hexapod in the beamline allowing for fine alignment of the sample with respect to the synchrotron beam. In this setup, it is possible to do in-situ X-ray scattering measurements during film growth. The cylindrical deposition chamber has a diameter of 600 mm and four 75-mm diameter sputter sources tilted with an angle of  $X^\circ$  towards the substrate normal. Between the sputter sources, a  $\mu$ -metal shielding is placed in order to extend the magnetic field closer to the substrate and minimise cross contamination. In front of the sputter sources, fast-acting shutters are mounted to control the sputtered flux. Enabling the growth of single layers, multilayers as well as the co-deposited samples grown in this work. The substrate is rotated during deposition, during this work at a constant rate of 7 rpm. The substrate table is electrically isolated in order to enable a negative substrate bias during film growth. The deposition chamber also allows for substrate heating during deposition, which has not been used during the depositions performed in this work.

# Chapter 5

## Instrumental aspects

### 5.1 Neutron Reflectometry

Neutron reflectometry (NR) is a technique to investigate structural properties of thin film multilayers. The physical principles behind this technique are described in chapter 2. The instrument used for NR is able to measure both specular and off-specular diffraction patterns simultaneously. These diffraction patterns can be used to obtain structural information about the sample that has been measured. Narrow Bragg peaks in the specular diffraction pattern for a multilayer indicate a regular periodicity [16] for example, and the distance between the peak widths can be used to calculate the period of the sample. In order to obtain quantitative information about the sample structure, the diffraction patterns can be fitted to mathematical simulations as covered in chapter ??.

#### 5.1.1 Neutron Instrument

The NR measurements in this work have been performed on the neutron reflectometer SuperADAM at Institut Laue-Langevin (ILL) [27]. The measurements have been performed at a neutron wavelength of 5.21 Å. A sketch of the instrument can be seen in figure 5.1. The monochromator consists of a beryllium filter which selects a single neutron wavelength. The slits collimate the beam, shaping the beam. The polarizer, magnetic field and the spin flipper are needed for polarised neutron reflectometry (PNR), which is not covered in this work. The mentioned polarizer, which is a solid state filter, can filter out unwanted wavelength harmonics as well [27]. The sample is kept in place at the sample holder, after which the reflected neutron beam travels through flight tubes towards the position sensitive detector (PSD) where off-specular and specular diffraction patterns can be measured simultaneously.

## 5. Instrumental aspects

---

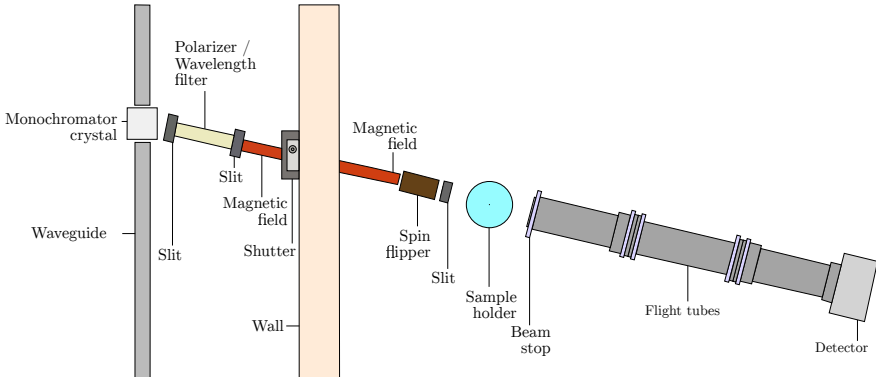


Figure 5.1: A top-down sketch of the SuperAdam reflectometer located at ILL.

### 5.1.2 Alignment procedure

## 5.2 X-ray Reflectometry

Like neutron reflectometry, X-ray reflectometry (XRR) is a non-destructive characterization technique that can be used to obtain structural properties of thin film multilayers. The physical principles follow the same formalisms as NR as described in chapter 2. While the underlying physics is very similar, NR does offer a few advantages over XRR. It is for example not possible to measure magnetic properties with XRR, and the short penetration length makes it much more difficult to measure bulk materials with this technique. Another useful property of neutrons is the fact that the scattering length for neutrons vary wildly per isotope as explained in section 2.2.1, making it possible to distinguish different isotopes of the same element. This also means that the scattering length for X-rays and neutrons are completely unrelated, this fact makes the combination of XRR and NR a very powerful technique as it gives two completely independent datasets with the same structural information. Combining these two techniques can therefore be an extremely powerful tool for mathematical simulations.

The XRR measurements in this work are performed on a Bragg-Brentano diffractometer, the corresponding geometric set-up can be seen in figure 5.2. The typically relevant angles are  $2\theta$ , which describes the angle between the direct beam and the reflected beam, and  $\omega$  which is the angle between the incoming beam and the sample surface. In order to retrieve specular

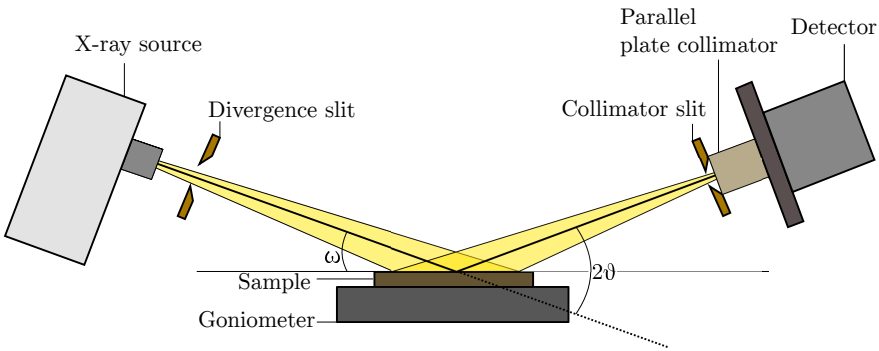


Figure 5.2: A sketch showing a typical Bragg-Brentano diffractometer and the relevant geometry.

diffraction patterns,  $\omega - 2\theta$  scans where done. In this setup,  $2\theta$  is measured from  $0^\circ - 12^\circ$  while  $\omega$  is kept at  $2\theta/2$ . The off-specular diffraction curves where measured by performing an  $\omega$  scan at a constant value for  $2\theta$ , typically at the first Bragg peak. The resulting intensity pattern, where  $\omega$  is varied at a constant angle for  $2\theta$  is often called a rocking curve. Off-specular diffraction gives quantitative information about the roughness profile in the multilayer.

### 5.2.1 X-ray Instrument

X-Ray reflectivity measurements were done using a Panalytical Empyrean diffractometer using a Cu-K $\alpha$  X-ray tube, giving rise to a wavelength of  $\lambda = 1.54\text{\AA}$ . On the incident side, a Ni filter was used to attenuate the K $_{\beta}$  radiation of the X-rays. A divergence slit of  $1/32^\circ$  was used to collimate the x-ray spot size. On the diffracted side, a parallel plate collimator has been used in combination with a collimator slit. The used detector is a PIXcel detector in 0D mode.

### 5.2.2 Alignment procedure

Depending on the relevant features in the diffraction pattern, a good alignment of the sample can be extremely important. In particular a proper correction of the beam overspill effect is extremely dependent on the alignment of the sample [28]. For a typical alignment procedure in this work,  $2\theta$  has been aligned before doing any measurements on the sample. This is done by doing a  $2\theta$  scan on the diffractometer around  $2\theta = 0^\circ$ , and setting the

resulting centre of the peak at zero degrees. Afterwards the sample can be aligned in the vertical  $z$ -direction by setting the direct beam at  $2\theta = 0^\circ$  and moving the sample into the beam until it blocks half of the direct beam intensity. Once this is done, the sample is tilted by changing the  $\omega$  angle such that the intensity reaches a maximum value. At this angle, the sample should be parallel to the beam. Since tilting the sample effectively changes the sample height, an additional alignment in the vertical  $z$ -direction is done until the sample blocks half of the sample beam. Finally, the  $2\theta$  is set to a low diffraction angle such that the detector measures the reflected beam. Usually this is done around the first Bragg peak of the multilayer. At this position the sample is tilted again around  $\omega$  after which the peak position of the obtained reflectivity curve is set to  $\omega = 2\theta/2$ . After this procedure has been carefully followed, the sample should be aligned and the measurement can begin.

### 5.3 The beam overspill effect

The spot size of the neutron beam grows with decreasing incidence angles and becomes infinitely large when the incidence angle approaches zero. A large part of the incident beam therefore does not reach the sample, leading to a reduction of intensity at lower angles. This is often called the beam overspill effect, this is illustrated in figure 5.3. The region where the intensity is reduced due to this effect is usually called the footprint of the sample. This effect needs to be calculated for using geometry and the beam profile. The experimentally measured curve can be expressed as:

$$E(\theta) = g(\theta)R(\theta) \quad (5.1)$$

Where  $g(\theta)$  is the attenuation factor due to the beam overspill effect, and  $R(\theta)$  describes the reflectivity curve in absence of this factor. The factor  $g(\theta)$  can be determined by considering the geometry of the beam which then reduces to [28] [29]:

$$\frac{\int_{-(L/2)\sin\theta}^{(L/2)\sin\theta} P(z)dz}{\int_{-(L/2)\sin\theta_{so}}^{(L/2)\sin\theta_{so}} P(z)dz} \quad (5.2)$$

where  $L$  is the size of the sample,  $\theta$  the incidence angle and  $\theta_{so}$  the angle where the beam spot size is exactly the same as the sample length.  $P(z)$  is the beam profile and can be expressed as

$$P(z) = Ae^{\frac{z^2}{2\sigma^2}}. \quad (5.3)$$

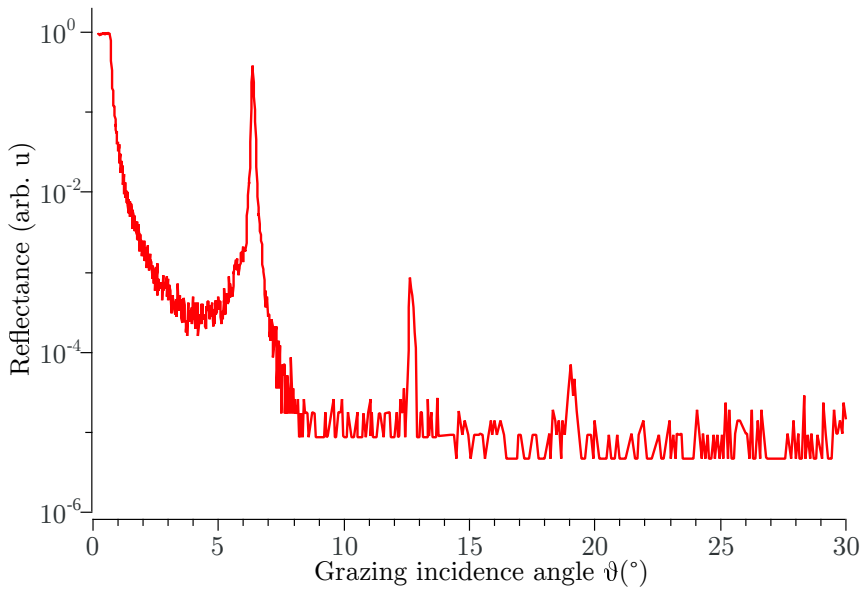


Figure 5.3: Part of the beam will not be reflected at low angles due to the infinite sample size. This leads to a reduced intensity at lower angles. (I am aware that this graph shows a sample with footprint correction. I'll fix that later)

Here  $A$  describes the amplitude and  $\sigma$  the half-width at half-maximum (HWHM) of the beam. For the analysis done in this work, the beam-overspill effect has been calculated using PySared, the data reduction software available at the neutron beamline at ILL. The footprint effect for X-rays has been calculated using the GenX software [30]



# Chapter 6

## Reflectivity Simulations

In order to obtain structural parameters for the samples, the experimental reflectivity curves need to be fitted to mathematical simulations for each sample. There are several possible mathematical descriptions that can be used, within this work there are two different descriptions that are applied based on the software that has been used. Specular reflectivity is used described using the Paratt recursion formula, whilst the off-specular simulation is described using the Born-approximation. Both of these formalisms are described in this chapter. Fitting of the specular parameters using Parrat recursion is done with the GenX software [30]. Off-specular simulations, which uses the Distorted Wave Born Approximation, are done using the BornAgain software [31].

### 6.1 Parrat recursion

The specular reflectivity of the samples is simulated using the Paratt recursion formalism. This description recursively accounts for the reflection from each subsequent interface in order to simulate the total intensity at detector. For a multilayer with a certain amount of layers, the reflectivity for the  $j$ 'th layer in the sample can be calculated using:

$$\chi_j = \frac{R_j}{T_j} = e^{-2ik_{z,j}z_j} \frac{r_{j,j+1} + \chi_{j+1}e^{2ik_{z,j}z_j}}{1 + r_{j,j+1}\chi_{j+1} + e^{2ik_{z,j}z_j}} \quad (6.1)$$

$R_j$  and  $T_j$  in this equation describe the reflected and transmitted amplitude for layer  $j$ . The fraction of these,  $\chi_j$  therefore describes the normalised intensity from each layer. The factor  $r_{j,j+1}$  is the Fresnel coefficient for the interface, and can be written as:

$$r_{j,j+1} = \frac{k_{z,j} - k_{z,j+1}}{k_{z,j} + k_{z,j+1}} \quad (6.2)$$

It follows from this description that this formalism is recursive, the reflectivity of layer  $j+1$  is required to calculate the reflectivity of the  $j$ 'th layer. To solve this equation, we can use  $T_1 = 1$  and  $R_{N+1} = 0$  as starting point, this equates to the incident wave having full transmission at  $T_1$ , and to no

## 6. Reflectivity Simulations

---

reflection from the substrate at  $R_{N+1}$ . This formalism is commonly used to simulate the specular reflection for neutrons and X-rays in reflectivity simulation software.

### 6.2 Born Approximation

The Born approximation (BA) was proposed as early as 1926 by Max Born. To get to this approximation, we may first start with the general time-independent Schrödinger equation:

$$\left( \frac{\hbar^2}{2m} \nabla^2 + V(\mathbf{r}) \right) \Psi(\mathbf{r}) = E\Psi(\mathbf{r}) \quad (6.3)$$

We can re-write this as:

$$(\nabla^2 + k^2) \Psi(\mathbf{r}) = \frac{2m^2}{\hbar^2} V(\mathbf{r}) \Psi(\mathbf{r}) \quad (6.4)$$

Where  $k^2 = \left(\frac{2m}{\hbar}\right)^2$ . The general solution to this equation can be expressed as an integral:

$$\Psi(\mathbf{r}) = \int G(\mathbf{r} - \mathbf{r}') V(\mathbf{r}') \Psi(\mathbf{r}') d^3\mathbf{r}' \quad (6.5)$$

The factor  $G$  in this equation is known as Green's function, which can be obtained by solving the point source equation:

$$(\nabla^2 + \mathbf{k}^2) G(\mathbf{r} - \mathbf{r}') = \delta(\mathbf{r} - \mathbf{r}') \quad (6.6)$$

Solving this for the Green's function gives us the integral form for the Schrödinger equation.

$$\Psi(\mathbf{r}) = e^{i\mathbf{k}_0 \cdot \mathbf{r}} - \frac{m}{2\pi\hbar^2} \int \frac{e^{i\mathbf{k}|\mathbf{r}-\mathbf{r}'|}}{|\mathbf{r} - \mathbf{r}'|} V(\mathbf{r}') \Psi(\mathbf{r}') d^3\mathbf{r}' \quad (6.7)$$

This equation can be solved approximately using the so-called Born series. The zero'th order solution of the Born approximation is given by a planar wave:

$$\Psi_0(\mathbf{r}) = e^{i\mathbf{k}_0 \cdot \mathbf{r}} \quad (6.8)$$

The first order solution is then given by inserting the solution for  $\Psi_0$  into the integral of the general equation expressed in equation 6.7. This then gives us:

$$\Psi_1(\mathbf{r}) = e^{i\mathbf{k}_0 \cdot \mathbf{r}} - \frac{m}{2\pi\hbar^2} \int \frac{e^{i\mathbf{k}|r-r_1|}}{|\mathbf{r} - \mathbf{r}_1|} V(\mathbf{r}_1) \Psi_0(\mathbf{r}_1) d^3\mathbf{r}_1 \quad (6.9)$$

$$= e^{i\mathbf{k}_0 \cdot \mathbf{r}} - \frac{m}{2\pi\hbar^2} \int \frac{e^{i\mathbf{k}|\mathbf{r}-\mathbf{r}_1|}}{|\mathbf{r}-\mathbf{r}_1|} V(\mathbf{r}_1) e^{i\mathbf{k}_0 \cdot \mathbf{r}} d^3 \mathbf{r}_1 \quad (6.10)$$

The second order can then be found by inserting this first order solution into equation 6.7. By continuing this way, any order can be obtained, but for most cases only the first order approximation is actually used.

### 6.2.1 The Distorted Wave Born Approximation

When the scattering intensity becomes very large, the assumption of a planar wave in the conventional BA no longer holds, scattering entities themselves can introduce perturbations into the field and the wave therefore needs to be described as a distorted wave, a superposition of a downwards and upwards travelling planar wave. This is the underlying principle of the Distorted Wave Born Approximation (DWBA), which is the formalism that is used to simulate off-specular scattering in this work. The described wave function has a distorted form that can be described as downward and upward travelling waves for both the scattered and incident waves [32]:

$$\psi_w(\mathbf{r}) = \psi_w^-(\mathbf{r}) + \psi_w^+(\mathbf{r}), w = i, f. \quad (6.11)$$

Where  $\psi_w^-$  describes the downwards wave while  $\psi_w^+$  describes the upwards wave. The relevant scattering elements can then be described using Dirac notation as follows [32]:

$$\langle \psi_i | \delta v | \psi_f \rangle = \langle \psi_i^- | \delta v | \psi_f^+ \rangle + \langle \psi_i^- | \delta v | \psi_f^- \rangle + \langle \psi_i^+ | \delta v | \psi_f^+ \rangle + \langle \psi_i^+ | \delta v | \psi_f^- \rangle \quad (6.12)$$

Where  $\delta v$  describes a perturbation on the scattering potential that the incident wave experiences. If we expand the left-hand side in the integral notation we get:

$$\langle \psi_i | \delta v | \psi_f \rangle = \int e^{i\mathbf{k}_i \cdot \mathbf{r}} \delta v e^{i\mathbf{k}_f \cdot \mathbf{r}} d^3 r = \int \delta v e^{i\mathbf{q} \cdot \mathbf{r}} d^3 r \quad (6.13)$$

Which gives us the Fourier transform of the perturbed potential  $\delta v$ , which is what is being measured at the detector. Note how the first term on the right-hand side in equation 6.12 simply describes the interaction with the downwards and the upwards wave, which is the usual term as used by the conventional BA. The additional terms are added upon this in the DWBA, and these describe the additional scattering effects for intense scattering. These terms are all illustrated in figure 6.1.

## 6. Reflectivity Simulations

---

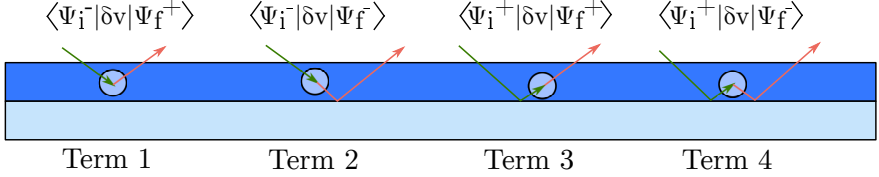


Figure 6.1: A representation of different terms that are taken into account for the DWBA. The first term is identical to the conventional BA, while the other three terms describe scattering events from the scattering entities themselves.

### 6.3 Sample description

The samples themselves need to be described in the simulation software in order to fit the experimental data with the simulated formalism. In order to do this in a meaningful way, some approximations need to be made. It is easy to describe the sample in as much detail as possible, and let the software fit for all possible parameters, but that leaves the possibility of overfitting, losing all physical meaning behind the result. It is therefore often better to make a robust and simple model, than a complicated model that fits better to the data. Mathematician George Box famously said, ‘all models are wrong, but some models are useful’. The task is not to find a model that gives a perfect fit to our data, but instead to find a model that gives useful information. In this work, this means a model that reliably gives physically correct information about the structural parameters of the sample. Within this work, the same description is used for all samples. A stack of an  $N$  amount of bilayers consisting of Ni and Ti are deposited on top of a Si substrate. A thin layer of  $\text{SiO}_2$  is assumed to be present between the Si substrate and the multilayer stack. Finally, a small oxide layer is assumed to be present on the top layer. A sketch describing this can be seen in figure 6.2. While the initial interface width of the Ni and Ti layers are considered independent from each other, the accumulation of the interface width is assumed to be equal. The total interface width for a Ni and Ti layer in the stack, is therefore determined by:

$$\sigma_{\text{Ti}} = A \cdot i + \sigma_{\text{Ti},i} \quad (6.14)$$

$$\sigma_{\text{Ni}} = A \cdot i + \sigma_{\text{Ni},i} \quad (6.15)$$

Where  $A$  is the accumulated interface width per bilayer,  $i$  indicates the position of the bilayer, and  $\sigma_{\text{Ni}}$  and  $\sigma_{\text{Ti}}$  describe the initial interface width

---

### Sample description



Figure 6.2: An illustration of the sample as described in the simulated model, not to scale. Each bilayer is given an index, dubbed  $i$ . For illustrative purposes, a limited amount of bilayers are drawn.

of Ni and Ti respectively.



# Chapter 7

## Multilayer Characterization

The multilayers in this work have been characterized with several techniques. Apart from X-ray- and neutron reflectometry, other techniques have been used as well. These techniques are described in this chapter.

### 7.1 Elastic Recoil Detection Analysis

The elemental composition of the multilayers in this work have been determined using Elastic Recoil Detection Analysis (ERDA). In this work, the Tandem Laboratory at Uppsala University has been used to perform such analysis. In ERDA, the sample is targeted by an ion beam with an energy in the order of tens of MeV. Atoms from the sample surface are ejected due to collision events between the energetic ions and the sample surface. Using the atomic number of the target elements and the energy of the backscattered ions, the recoil can be measured and analysed to obtain compositional information. Such an obtained ERDA spectrum can be observed in figure 7.1. Upon collision, light elements are most likely to be ejected in the forward direction. This technique is less suitable for heavier elements as they do not recoil as easily and overlap with backscattered ions [25]. In this work, a primary  $^{127}\text{I}^{8+}$  beam with an energy of 36 MeV has been used at an incident angle of 67.5° relative to the surface normal, the energy detector was placed at a recoil scattering angle of 45°. The measured spectrum has been analysed using the Potku software [33] in order to determine the elemental composition of the sample.

### 7.2 X-ray Photoelectron Spectroscopy

X-Ray Photoelectron Spectroscopy (XPS) has been used in this work to analyse the bonding of the boron and carbon atoms that are present in the film. XPS provides qualitative and quantitative information about the chemical composition of the sample near the surface. This technique is based on the photoelectric effect [34], electrons on the sample are ejected by an incident X-ray beam with a certain kinetic energy  $E_k$  that is measured at

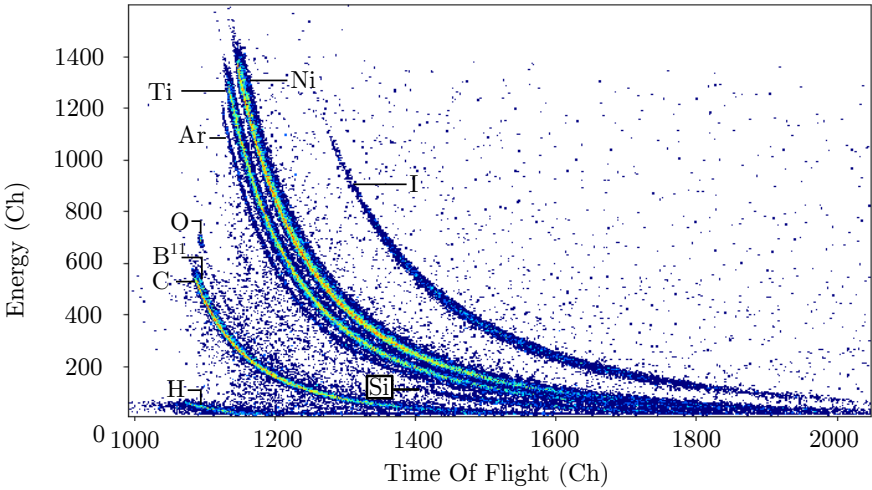


Figure 7.1: An example of results as obtained by ERDA. The different elements that are present in the sample are observed as "banana peaks", the curved signals that are visible in the graph. Note how the iodine signal are backscattered ions from the target beam, there is no iodine present in the measured sample.

the detector. The binding energy  $E_b$  is related to this kinetic energy as:

$$E_b = E_{\text{XPS}} - (E_k + \phi) \quad (7.1)$$

Where term  $E_{\text{XPS}}$  represents the energy of the incident X-rays. The function  $\phi$  is the work function for the instrument, this represents the minimum energy that is needed to remove an electron from the instrument [35]. Equation 7.1 can therefore be used to see which chemical bonds were present in the sample, what makes this particular powerful is that it does not just show the elemental composition of the sample but also how the elements were bonded.

### 7.3 Transmission Electron Microscopy

Transmission electron microscopy (TEM) has been used to get a direct view of the structural characteristics, as well as the roughness propagation throughout the entire sample. TEM is an electron microscopy technique that is able to

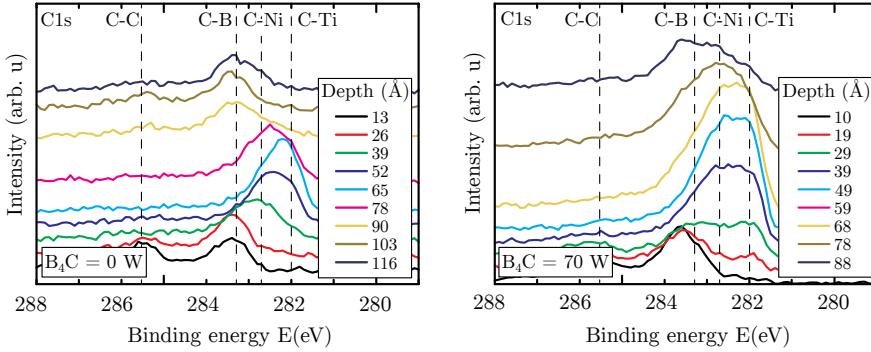


Figure 7.2: The C1s XPS spectrum for two deposited samples. The left-hand side shows a Ni/Ti sample with a power of 0 W to the  $^{11}\text{B}_4\text{C}$  magnetron, while the right-hand side shows a Ni/Ti sample with a power of 70 W to the  $^{11}\text{B}_4\text{C}$  magnetron.

obtain structural information from samples that are thin enough to transmit electrons. In a simplistic sense, TEM can be compared to a slide projector, where the sample itself is used as the slide and the electron beam is the beam of light [22]. The interaction of the electrons with the sample form an image which is magnified by a lens. The high magnification that is obtainable with TEM is a result from the very small wavelengths that are used. There are different modes of operation that determine the beams reaching the objective lens are processed. The ones that are relevant to this work are further covered here, all discussed modes of operation are shown in figure 7.3.

### 7.3.1 Bright-field imaging

Bright-field (BF) imaging is known as the conventional TEM [22]. With this mode of operation the diffracted beam is excluded and only the central transmitted beam is allowed to pass through. This is done by placing an aperture in the back focal plane of the objective lens. For BF imaging, the obtained contrast in the resulting image is a result of mass-absorption and the interference from transmitted electrons. As heavier elements absorb more, a multilayer with heavy/light elemental layers will respectively appear as dark/bright layers in the obtained image. Similarly, thicker layers will appear darker than thin layers [25].

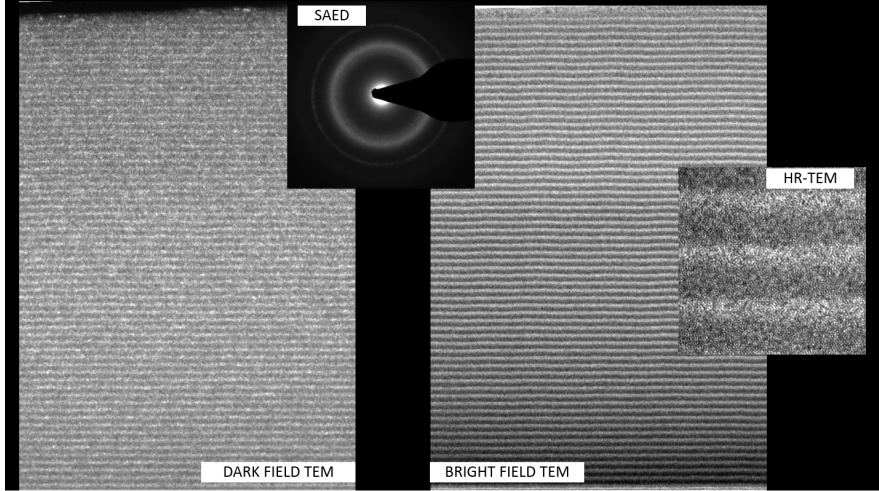


Figure 7.3: A TEM measurement of one of the samples that has been deposited in this work. The modes of operations that have been discussed in this text are shown in the figure.

### 7.3.2 Dark-field imaging

With dark-field (DF) imaging, one of the diffracted beams is chosen. In this case, an aperture is inserted that blocks both the transmitted central beam as well as the other diffracted beams. With this mode of operation, the obtained contrast is primarily a result of diffraction [25]. As this mode of operation is dependent on diffraction conditions, the resulting contrast will be dependent on the formation of crystallites.

### 7.3.3 High Resolution Transmission Electron Microscopy

To obtain images with an even higher magnification, high resolution transmission electron microscopy (HR-TEM) can be used. With this mode of operation, both the scattered and transmitted beams are used in order to form an interference image [25]. This technique is based on the phase shift that the electron wave experiences when interacting with the atoms in a sample. The interference pattern in the image plane gives rise to the contrast in HR-TEM images. Small features such as dislocations can be recorded with this technique due to the strong interaction between electrons

and the atoms in the sample [36].

#### 7.3.4 Selected Area Electron Diffraction

Selected Area Electron Diffraction (SAED) patterns are diffraction patterns of a selected area within one sample. To obtain such a pattern, a special aperture is inserted into the image plane to select an area of the sample. The diffraction pattern can be magnified and viewed by the TEM. Crystalline materials give rise to diffraction spots, while polycrystalline and amorphous materials give diffraction rings of varying sharpness and width, note how these rings can be observed as well in figure 7.3. Using this mode of operation, strains and texture deviations can be found for individual grains [22].



# Chapter 8

## Summary of the results

Within this thesis, Ni/Ti samples have been deposited with- and without  $^{11}\text{B}_4\text{C}$  co-deposition. These samples have been analysed using several techniques, and compared to each other.

### 8.1 Pure Ni/Ti multilayers

Pure Ni/Ti multilayers have been deposited without any  $^{11}\text{B}_4\text{C}$  co-deposition during growth. These samples are primarily meant as a control group, in order to monitor the improvement as a result from the  $^{11}\text{B}_4\text{C}$  co-deposition on the reflectivity performance. These samples have been deposited at sputter deposition system at Petra III in Hamburg, described in subsection 4.5. The samples that are discussed in this work are grown with a split-bias scheme, using an initial bias at -30 V to grow a buffer layer followed by a high bias at -100 V for the rest of the layer. The magnetron powers that have been used are 20 W and 60 W for the Ni- and Ti target respectively.

#### 8.1.1 Structural parameters

Structural parameters of the samples have been obtained by fitting the measured NR and XRR data to a model simulation of the multilayer. In this model, any accumulation of interface width is assumed to be linear and equal for both multilayers. The resulting fit shows an average initial width of 6.4 Å for the sample, with an increase of 0.03 Å per bilayer, meaning the total interface width has grown to 9.4 Å after 100 bilayers. The specular diffraction pattern shows a slight broadening of the Bragg peaks, indicating an increase in layer thickness throughout the layer. The simulated fit to the experimental data shows an increase of 0.002 Å per bilayer. The obtained period was 45.8 Å. The sample has been measured with TEM microscopy as well. The TEM measurement confirms the findings from the model simulation, with abrupt interfaces and very limited roughness accumulation.

## 8.2 Ni/Ti multilayers containing $^{11}\text{B}_4\text{C}$

The samples that have been co-deposited with  $^{11}\text{B}_4\text{C}$  are grown at the deposition system at Petra III in Hamburg. The magnetron powers that were used are 20 W, 60 W and 35 W for the Ni, Ti, and  $^{11}\text{B}_4\text{C}$  target respectively. These samples were grown with a split-bias scheme, using an initial bias at -30 V to grow a buffer layer followed by a high bias at -100 V for the rest of the layer. These samples were analysed using ERDA in order to obtain information about the elemental composition for the multilayer. These measurements indicate that the sample contains about about 3.6% C and 21%  $^{11}\text{B}$ . The sample also contains about 1% Ar, which comes from the sputtering gas that is used during deposition. The B to C ratio is slightly higher than expected from a pure  $^{11}\text{B}_4\text{C}$  target. The reason behind this remains unknown, but these findings have been confirmed using Rutherford Backscattering Spectroscopy (RBS) as well. A possible explanation could be an unexpected elemental composition in the target that was used.

### 8.2.1 Structural parameters

Structural parameters of the samples that were co-deposited with  $^{11}\text{B}_4\text{C}$  have been obtained by a combined fit of NR and XRR data on a model simulation of this multilayer. The same model has been used for these samples as for the pure Ni/Ti samples, so any accumulation in interface width is assumed to be linear and equal throughout the multilayer. The SLD has been calculated using the elemental composition obtained by ERDA where the density for each layer has been calculated using a simple rule of mixtures for the bulk densities for each element. The resulting fit to this model does not show any roughness accumulation throughout the sample. The obtained interface width has an average value of 4.5 Å for the multilayer, which is a clear improvement when compared to the pure Ni/Ti samples. The specular diffraction pattern shows a slight broadening of the Bragg peaks, indicating an increase in layer thickness throughout the layer. The simulated fit to the experimental data shows an increase of 0.002 Å per bilayer. The obtained period was 47.0 Å. These samples were measured with TEM as well, the TEM micrographs for this sample is shown in figure 7.3. These measurements are in line with the obtained fit to the simulated model, with very abrupt layers and no obvious sign of an increase in interface width throughout the layer. The first Bragg peak of specular NR measurements is shown in figure 8.1 for the sample with- and without  $^{11}\text{B}_4\text{C}$  co-deposition. The total reflectivity at the first Bragg peak is about 2.2 times higher for the

sample that has been grown with  $^{11}\text{B}_4\text{C}$  co-deposition. The inset shows the rocking curves for the NR measurements for both samples. Note how the sample that has been co-deposited with  $^{11}\text{B}_4\text{C}$  has a higher diffuse signal. This could be the result of lower intermixing, increasing the contribution from correlated scattering from the horizontal plane in the sample.

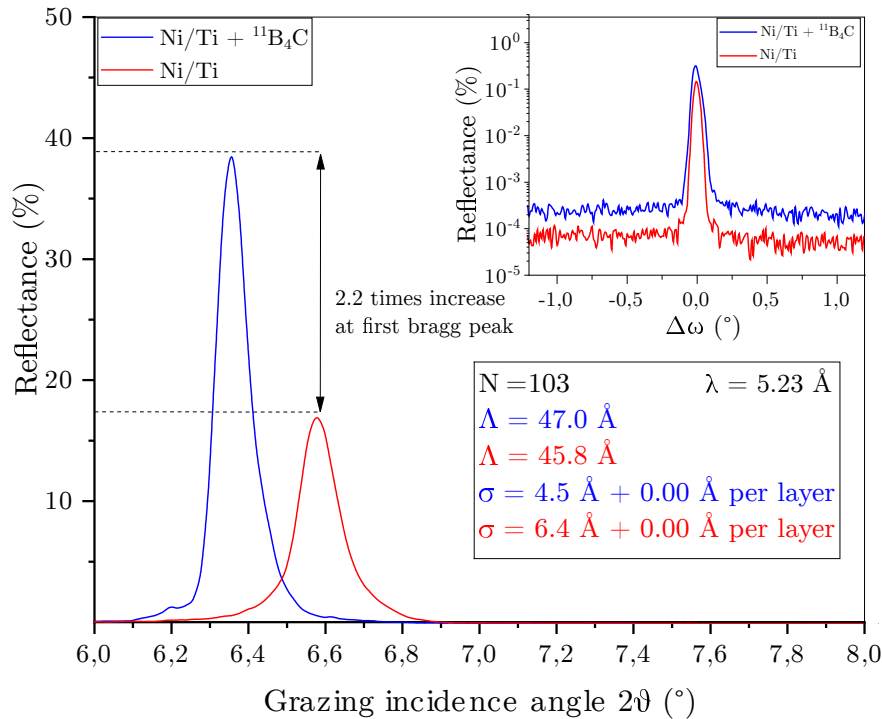


Figure 8.1: Neutron Reflectometry measurements for Ni/Ti samples at the first Bragg peak, with and without  $^{11}\text{B}_4\text{C}$  co-deposition.



# Chapter 9

## Outlook

### 9.1 Ni/Ti multilayers

Initial results described in chapter 8 show a clear improvement in interface width for the samples that have been co-deposited with  $^{11}\text{B}$ . There are however several aspects where this technique could be further improved. Initial depositions have been made using a magnetic coil in the deposition chamber to attract ions during layer growth. The resulting samples show a clear further improvement in reflectivity.

These samples have been measured at the neutron beamline at ILL as well, and a clear improvement in Neutron reflectivity can be observed. These samples do give a more difficult fit to experimental data, and the analysis has not been completed in time in order to be included in this thesis. Further experimental work needs to be done as well during the growth process. Due to the high contrast in neutron SLD for Ti and  $^{11}\text{B}_4\text{C}$ , a large improvement in reflectivity performance could be obtained by limiting the amount of  $^{11}\text{B}_4\text{C}$  in the Ti-layer.

Finally, a greater understanding is needed of the sample structure in the horizontal plane. Preliminary work has been done on off-specular simulations in order to get a qualitative understanding of the obtained rocking curve, but a proper off-specular fit to the experimental data has proven to be rather difficult due to the low amount of features in the rocking curve. Such an analysis would therefore require additional experimental analysis.

### 9.2 Co/Ti multilayers

While these results show great potential for non-polarising neutron multilayers, the same techniques could be applied to polarising multilayers as well.



# Chapter 10

## Summary of the papers

### 10.1 Paper I

In this work we investigated a novel magnetron sputter growth technique where 11B4C co-deposition has been combined with a split-bias scheme in order to reduce interface width at Ni/Ti multilayers. Combined fits to experimental XRR and NR data indicate interface widths of 4.5 Å without any accumulated roughness when the sample is co-deposited with 11B4C. This is a significant reduction from the deposited sampled with pure Ni/Ti, which show a nominal interface width of 6.3 Å and an accumulation of 0.03 Å per bilayer. This improved interface width offers very good prospects for high-performance supermirrors with high-m values, as well as for neutron instruments for cold neutrons where thinner interface widths are required. Since neutron multilayers are such essential and crucial elements in any intended instrumentation, even the slightest improvement of the performance will have an immediate and large impact on all research using those instruments.

### 10.2 Paper II

Ni/Ti is the materials system of choice for broadband neutron multilayer supermirrors. The reflected absolute intensity as well as neutron energy range from state-of-the-art mirrors are hampered by a Ni/Ti interface width, typically 0.7 nm (caused by nanocrystallites, interdiffusion, and/or intermixing), limiting the optical contrast across the interface as well as limiting the minimum usable layer thickness in the mirror stack. In this work we explore elimination of nanocrystallites by amorphization through boron-carbon doping in combination with interface smoothening by modulation of ion-assistance during magnetron sputter deposition of individual Ni and Ti layers, ranging from 0.8 nm to 6.4 nm in thickness. In situ high-energy synchrotron wide angle X-ray scattering (WAXS) revealed an effective hindering of Ni/Ti crystallization through a minute concurrent B4C flux during growth. Post-growth X-ray reflectivity (XRR) confirmed the incorporation of B4C but also showed that interface widths deteriorated when a constant substrate bias of -30 V was used. However, XRR showed that

## 10. Summary of the papers

---

interface widths in B<sub>4</sub>C-doped multilayers improved significantly, compared to those in pure Ni/Ti multilayers, by employing a two-stage substrate bias, where the initial 1 nm of each layer was grown with -30 V substrate bias, followed by -100 V bias for the remaining part of the layer. The present results shows that B<sub>4</sub>C doping of Ni/Ti multilayers leads to significantly smaller interface widths when combined with engineered interfaces through temporal control of the substrate bias. Consequently, a significant improvement of neutron supermirror performance can be expected by employing this technique using <sup>11</sup>B isotope-enriched B<sub>4</sub>C source material.

# Bibliography

- [1] K. Lefmann. *Neutron scattering: Theory, instrumentation, and simulation*. Niels Bohr Institute, University of Copenhagen, 2017.
- [2] F. L. Fernandez-Alonso and D. L. Price. *Neutron scattering: applications in biology, chemistry, and materials science*. Academic Press, an imprint of Elsevier, 2017.
- [3] S. Parker and P. Collier. “Applications of Neutron Scattering in Catalysis”. In: *Johnson Matthey Technology Review* 60 (2016-04), pp. 132–144. DOI: 10.1595/205651316X691230.
- [4] T. Brückel et al. *Neutron scattering*. Vol. 39. Forschungszentrum, Zentralbibliothek, 2012. URL: <https://juser.fz-juelich.de/record/155062/files/FZJ-2014-04247.pdf>.
- [5] J. W. Lynn. “Magnetic Neutron Scattering”. In: *Characterization of Materials*. American Cancer Society, 2012, pp. 1–14. ISBN: 9780471266969. DOI: <https://doi.org/10.1002/0471266965.com101.pub2>.
- [6] A. Belushkin. “Neutron scattering: history, present state and perspectives”. In: *Joint Institute for Nuclear Research* 152 (1999).
- [7] G. S. Bauer. *Physics and technology of spallation neutron sources*. 1998-08.
- [8] G. S. Bauer. “Neutron sources”. In: Neutron scattering. Switzerland: Paul Scherrer Institut, 1993, p. 384. URL: [http://inis.iaea.org/search/search.aspx?orig\\_q=RN:25007731](http://inis.iaea.org/search/search.aspx?orig_q=RN:25007731).
- [9] P. Staron et al. *Neutrons and Synchrotron Radiation in Engineering Materials Science: From Fundamentals to Applications*. Second Edition. Wiley-VCH, 2017. ISBN: 9783527335923.
- [10] H. Lengeler. “The European spallation source study”. In: *Nuclear Instruments and Methods in Physics Research Section B: Beam Interactions with Materials and Atoms* 139.1 (1998), pp. 82–90. ISSN: 0168-583X. DOI: [https://doi.org/10.1016/S0168-583X\(97\)00975-0](https://doi.org/10.1016/S0168-583X(97)00975-0).
- [11] R. Garoby et al. “The European Spallation Source Design”. In: *Physica Scripta* 93.1 (2017-12), p. 014001. DOI: 10.1088/1402-4896/aa9bff.

## Bibliography

---

- [12] D. Liu et al. “Demonstration of a novel focusing small-angle neutron scattering instrument equipped with axisymmetric mirrors”. In: *Nature communications* 4 (2013-09), p. 2556. DOI: 10.1038/ncomms3556.
- [13] F. Cousin and A. Menelle. “Neutron Reflectivity”. In: *EPJ Web of Conferences* 104 (2015), p. 01005. DOI: <https://doi.org/10.1051/epjconf/201510401005>.
- [14] A. J. Jackson. *Introduction to Small-Angle Neutron Scattering and Neutron Reflectometry*. NIST Center for Neutron Research, 2008.
- [15] B. Hammouda. *A Tutorial on Small-Angle Neutron Scattering from Polymers*. NIST Center for Neutron Research. URL: [https://www.ncnr.nist.gov/programs/sans/pdf/polymer\\_tut.pdf](https://www.ncnr.nist.gov/programs/sans/pdf/polymer_tut.pdf) (visited on 2021-01-04).
- [16] T. Shinjo and T. Takada. *Metallic superlattices: artificially structured materials*. Studies in Physical and Theoretical Chemistry 49. Elsevier, 1987.
- [17] C. Kittel. *Introduction to Solid State Physics*. Fifth Edition. Wiley, 1976. ISBN: 0471490245.
- [18] M. Birkholz. *Thin Film Analysis by X-ray Scattering*. Wiley-VCH, 2006. ISBN: 9783527310524.
- [19] F. Eriksson. “Soft X-ray multilayer mirrors”. PhD thesis. Linköping University, 2004.
- [20] E. Spiller. “Characterization of multilayer coatings by X-ray reflection”. In: *Revue de Physique Appliquee* 23.10 (1988), pp. 1687–1700. DOI: 10.1051/rphysap:0198800230100168700.
- [21] R. Alvarez et al. “On the Deposition Rates of Magnetron Sputtered Thin Films at Oblique Angles”. In: *Plasma Processes and Polymers* 11.6 (2014), pp. 571–576. DOI: 10.1002/ppap.201300201.
- [22] M. Ohring. *Materials science of thin films: deposition and structure*. Elsevier, 2002.
- [23] D. Depla, S. Mahieu, and J. Greene. “Sputter Deposition Processes”. In: *Handbook of Deposition Technologies for Films and Coatings* (2010). DOI: 10.1016/B978-0-8155-2031-3.00005-3.
- [24] K. Järrendahl. “Growth and characterization of amorphous Ge/Si multilayered structures”. PhD thesis. Linköping University, 1995.
- [25] N. Ghafoor. “Materials science of multilayer X-ray mirrors”. PhD thesis. Linköping University, 2008.

- [26] J. L. Schroeder et al. “Industry-relevant magnetron sputtering and cathodic arc ultra-high vacuum deposition system for in situ x-ray diffraction studies of thin film growth using high energy synchrotron radiation”. In: *Review of Scientific Instruments* 86.9 (2015), p. 095113. DOI: 10.1063/1.4930243.
- [27] A. Devishvili et al. “SuperADAM: Upgraded polarized neutron reflectometer at the Institut Laue-Langevin”. In: *Review of Scientific Instruments* 84.2 (2013), p. 025112. DOI: 10.1063/1.4790717.
- [28] A. Das et al. “Data-reduction procedure for correction of geometric factors in the analysis of specular X-ray reflectivity of small samples”. In: *Journal of Applied Crystallography* 51.5 (2018), pp. 1295–1303. DOI: 10.1107/S1600576718010579.
- [29] A. Gibaud, G. Vignaud, and S. K. Sinha. “The correction of geometrical factors in the analysis of X-ray reflectivity”. In: *Acta Crystallographica Section A* 49.4 (1993), pp. 642–648. DOI: 10.1107/S0108767392013126.
- [30] M. Björck and G. Andersson. “GenX: an extensible X-ray reflectivity refinement program utilizing differential evolution”. In: *Journal of Applied Crystallography* 40.6 (2007), pp. 1174–1178. DOI: <https://doi.org/10.1107/S0021889807045086>.
- [31] G. Pospelov et al. “BornAgain: software for simulating and fitting grazing-incidence small-angle scattering”. In: *Journal of Applied Crystallography* 53.1 (2020), pp. 262–276. DOI: 10.1107/S1600576719016789.
- [32] J. Burle et al. *BornAgain. Software for simulating and fitting X-ray and neutron small-angle scattering at grazing incidence. User Manual*. Forschungszentrum Jülich GmbH, 2018-12. URL: <http://apps.jcns.fz-juelich.de/src/BornAgain/PhysicsManual.pdf> (visited on 2021-01-21).
- [33] K. Arstila et al. “Potku – New analysis software for heavy ion elastic recoil detection analysis”. In: *Nuclear Instruments and Methods in Physics Research Section B: Beam Interactions with Materials and Atoms* 331 (2014). 11th European Conference on Accelerators in Applied Research and Technology, pp. 34–41. ISSN: 0168-583X. DOI: <https://doi.org/10.1016/j.nimb.2014.02.016>. URL: <http://www.sciencedirect.com/science/article/pii/S0168583X14002717>.
- [34] A. Einstein. “Über einen die Erzeugung und Verwandlung des Lichtes betreffenden heuristischen Gesichtspunkt”. In: *Annalen der Physik* 322.6 (1905), pp. 132–148. DOI: <https://doi.org/10.1002/andp.19053220607>.

## Bibliography

---

- [35] P. van der Heide. *X-ray Photoelectron Spectroscopy: An introduction to Principles and Practices*. 1st ed. Wiley, 2011. ISBN: 9781118062531.
- [36] R. Li et al. “A Review of Transmission Electron Microscopy of Quasicrystals—How Are Atoms Arranged?” In: *Crystals* 6.9 (2016). ISSN: 2073-4352. DOI: 10.3390/crust6090105.

# Papers



# Paper I

Include title and authors and stuff.

# Synthesis of $^{11}\text{B}_4\text{C}$ containing Ni/Ti multilayers and characterization using combined X-ray and neutron reflectometry

**Sjoerd Broekhuijsen,<sup>1</sup>** Fredrik Eriksson,<sup>1</sup> Naureen Ghafoor,<sup>1</sup> Martin Wess,<sup>1</sup> Alexei Vorobiev,<sup>2</sup> Jens Birch<sup>1</sup>

<sup>1</sup> Department of Physics, IFM, Linköping University, SE-581 83 Linköping, Sweden

<sup>2</sup> Institut Max von Laue—Paul Langevin, 71 avenue des Martyrs, 38000 Grenoble, France

## Abstract

The ultimate performance of Ni/Ti neutron multilayer mirrors is crucially dependent on a high optical contrast and a minimal achievable layer thickness in the multilayers. However, these are currently limited by a finite interface width between the individual layers. As the reflectivity of a multilayer depends exponentially on the square of the interface width, even a modest improvement of these factors can lead to a significant increase in reflectivity performance of neutron optical components such as neutron supermirrors.

In this work we have incorporated low-neutron-absorbing  $^{11}\text{B}$  and C during deposition to inhibit the formation of nanocrystals and limit interdiffusion in Ni/Ti multilayers. To overcome accumulated roughness caused by limited adatom mobility we employed a modulated ion-assistance scheme during magnetron sputter deposition in which the initial part of each layer is grown with a low substrate bias voltage of -30 V while the remainder of the layer is grown using a higher bias of -100 V. This modulates the energy of ions attracted from the process plasma in a way that minimizes intermixing into the previous layer and then stimulates adatom mobility to create a smooth top surface before deposition of the next layer[2].

Multilayers deposited with and without  $^{11}\text{B}_4\text{C}$  co-sputtering have been investigated using a combination of Elastic Recoil Detection Analysis (ERDA) to determine the composition, and X-ray reflectivity (XRR) and neutron reflectivity (NR) for structural analysis and to determine reflectivity performance. A model representing the samples has been created using the GenX reflectivity fitting software[3], and the relevant structural parameters are fitted simultaneously to both X-ray and neutron reflectivity data. The resulting fit shows an elimination of accumulated roughness for the samples containing  $^{11}\text{B}_4\text{C}$ , as well as a higher overall neutron reflectivity, whereas the sample with pure Ni/Ti has a roughness accumulation of 0.03 Å per bilayer. The nominal interface width of the samples has been found to be 4.5 Å, compared to the current state-of-the-art of 7 Å [1]. TEM measurements on these samples are in agreement with the parameters found by the fitted XRR and NR data. Simulations based on these achieved interface widths suggest the total neutron transmission for a typical Ni/Ti supermirror waveguide with 10 reflections to increase with more than 7 times, therefore offering promise for significantly improved neutron flux at (future) neutron instrument stations.

## Introduction

Neutron scattering is a non-destructive analytical technique which can be a powerful tool to investigate a range of physical properties. This technique offers some interesting advantages, among others for the study of bulk materials, magnetic properties and condensed matter. Neutron scattering however is a signal limited technique: even the most brilliant neutron sources have a flux that is orders of magnitudes lower than the attainable flux for X-rays. By improving the optical components used at a neutron source, one can in principle increase the neutron flux at experiment without constructing more powerful neutron sources. Indeed, the largest increase of neutron flux at experiment is expected to come from the improvement of neutron optical components.

Ni/Ti multilayers are the most conventional system choice for neutron multilayer mirrors. The reflectivity performance of such mirrors is dependent on the interface width of these multilayers in accordance to a Debye-Waller factor as given in equation 1:

$$R = R_0 e^{-\left(2 \pi m \frac{\sigma}{\Lambda}\right)^2}$$

It follows that the reflectivity is exponentially dependent on the square of the interface width, so even a modest improvement can lead to a significant increase of reflectivity performance of a neutron supermirror. The interface width between the layers of a neutron supermirror are caused by a combination of nanocrystallites, formation of intermetallics, intermixing, and interdiffusion between sequent layers in the mirror. [1]

Here we present a novel magnetron sputter growth technique that is predicted to substantially increase the reflectivity in neutron optical components such as supermirrors, allowing for a higher flux at the experiment. By incorporating low-neutron-absorbing  $^{11}\text{B}_4\text{C}$  during deposition, the formation of nanocrystals was inhibited and X-ray amorphous Ni/Ti multilayers were obtained. However, the addition of  $^{11}\text{B}_4\text{C}$  severely limits the adatom surface mobility during the sputtering process and deposited atoms will stick directly to the landing sites creating rough layers. This problem has now been overcome using a modulated bias scheme during deposition. Multilayers deposited with and without  $^{11}\text{B}_4\text{C}$  co-sputtering have been investigated using a combination of Elastic Recoil Detection Analysis (ERDA) to determine the composition, and X-ray reflectivity (XRR) and neutron reflectivity (NR) for structural analysis and reflectivity performance. Initial findings show a significant increase of reflectivity at the first Bragg peak as well as a total elimination of accumulated roughness for the samples containing  $^{11}\text{B}_4\text{C}$ .

At some point I need to fit in some off-specular theory as well, maybe here in introduction?

### Experimental Details

Thin film multilayers of Ni/Ti, co-deposited with  $^{11}\text{B}_4\text{C}$  have been deposited onto Si (100) substrates using ion-assisted DC magnetron sputter deposition. [INSERT DETAILS ABOUT PETRA III HERE].

Multilayer thin films of pure Ni/Ti and those doped with  $\text{B}_4\text{C}$  have been deposited onto Si (100) substrates using ion-assisted DC magnetron sputter deposition. The 600-mm-diameter cylindrical deposition chamber is equipped with four 75-mm-diameter sputter sources tilted with an angle of  $X^\circ$  towards the substrate normal with a target-to-substrate distance of 150 mm. Between adjacent sputter sources high magnetic permeability  $\mu$ -metal shielding is used to minimize cross contamination as well as to extend the magnetic field closer to the substrate. In front of the sputter sources fast-acting shutters allow for control of the sputtered flux and enables single layers, multilayers, as well as co-sputtered layers to be deposited.

The  $10 \times 10 \times 0.5 \text{ mm}^3$  substrates were rotating around the sample normal at constant rate of 7 rpm, directly in line of sight of all sputter sources. The substrate table was electrically isolated enabling a negative substrate bias voltage to be applied during growth. Although substrate heating was available depositions were performed at ambient growth temperatures ( $< 50^\circ\text{C}$ ). The chamber was evacuated to a base pressure of X Pa (Y Torr) using a dual turbo setup and was equipped with a loadlock to maintain a good vacuum and allow for easy sample exchange. The deposition system is described in more detail elsewhere [5].

Ultra-high purity argon gas ( $> 99.999998\%$ ) was introduced to a working pressure of 3 mTorr (0.4 Pa), as measured with a capacitance manometer. Target discharges were established with constant-power power supplies, and discharge powers of 20 W and 60 W, as measured with closed shutters, were used for Ni and Ti, respectively. This yielded Ni and Ti deposition rates of about 0.36 and 0.39 nm/s as determined from hard X-ray reflectivity measurements of single layer films. For  $\text{B}_4\text{C}$ , a discharge power of 35 W was used.

As a proof of concept, two of these samples have been measured using various techniques in order to investigate the structural properties. One sample consisting of 104 bilayers of pure nickel and titanium, and one sample with the same amount of bilayers where the nickel-titanium bilayers have been continuously co-deposited with  $^{11}\text{B}_4\text{C}$ . Apart from the inclusion of  $^{11}\text{B}_4\text{C}$ , both samples have been deposited under the same conditions as described above.

The elemental composition of the films was determined using time-of-flight energy recoil detection analysis (ToF-E ERDA) at the Tandem Laboratory at Uppsala University. A primary beam of  $^{27}\text{Al}^{8+}$  was used with an energy of 36 MeV at an incident angle of  $67.5^\circ$  relative to the surface normal, the energy detector was placed at a recoil scattering angle of  $45^\circ$ . A detailed description of the experimental set-up is given elsewhere. The measured data has been analysed using the Potku software in order to determine the atomic concentrations.

An analytical Tecnai G2 UT FEG microscope operating at 200 kV for a point-to-point resolution of 0.19 nm was used for transmission electron microscopy (TEM) studies. Microstructure and layer definition of Ni/Ti and Ni/Ti doped with  $\text{B}_4\text{C}$  multilayers were studied using both bright field and dark field imaging as well as high resolution cross-sectional TEM. Dark field imaging was used as an approach to effectively highlight crystalline regions in the sample, while high-resolution TEM was used to investigate the layered structure in the multilayers containing the thinnest periods. The cross-sectional samples were prepared using mechanical grinding and polishing followed by low-energy ion-beam milling using a Gatan precision ion polishing system.

Neutron reflectometry measurements were performed for a series of samples at Institut Laue–Langevin in Grenoble with the SuperAdam refractometer at a monochromatic wavelength of 5.23 Å. The distance from the sample to detector was 150 cm. Both the specular and off-specular signal has been obtained simultaneously in this set-up. The samples have been measured in a range of 0°-15° with 0.01°/step using a constant acquisition time per step of XX, leading to a total acquisition time of 9h20m. Footprint correction has been applied to the specular beam using a trapezoid beam with a width of XX mm, and the data has been normalized to the resulting critical angle.

X-Ray reflectivity measurements were done using a Panalytical Empyrean diffractometer using a Cu X-ray tube. On the primary side, a 1/32° divergence slit has been used, while a parallel plate collimator has been used in combination with a collimator slit on the refracted side with a PIXcel detector in 0D mode. Reflectivity of single Ni/Ti multilayers doped with B<sub>x</sub>C were measured in the range 0°-10° with a step size of 0.01°/step and a collection time of 1.75 s, giving a total measurement time of ~30 minutes.

Structural analysis has been performed by fitting the obtained XRR and NR data simultaneously to a model created with the GenX reflectivity fitting software which uses the Paratt recursion formula to simulate specular reflectivity. All samples are described using the same model description. A stack of a fixed amount of bilayers is described on top of a Si substrate. A thin layer of native SiO<sub>2</sub> is described between on top of the substrate, as well as a thin layer of NiO<sub>2</sub> on top of the multilayer stack.

While the initial interface width between the Ni- and Ti layers are considered to be independent from each other, the increase of interface width after each bilayer is considered equal for both layers. The total interface width for a Ni and Ti layer in the stack is therefore determined by:

$$\begin{aligned}\sigma_{\text{Ni}} &= A \cdot i + \sigma_{\text{Ni},i} \\ \sigma_{\text{Ti}} &= A \cdot i + \sigma_{\text{Ti},i}\end{aligned}$$

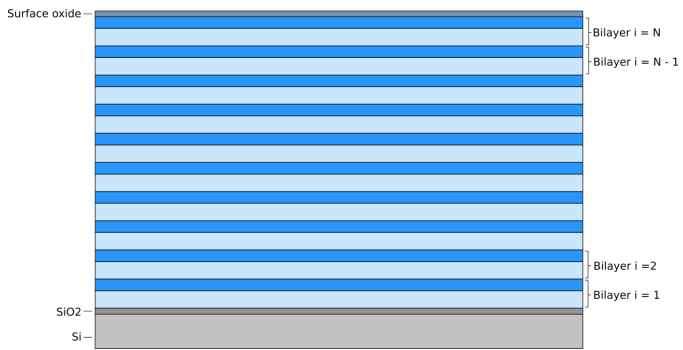
Where A is the accumulated interface width per bilayer, the letter i indicates the position of the bilayer in the stack, and  $\sigma_{\text{Ni},i}$  and  $\sigma_{\text{Ti},i}$  describe the initial interface width of Ni and Ti respectively. A sketch of this model can be seen in figure X. The samples also have a slight drift in interface thickness throughout the layer, which accounts for a slight peak broadening at higher q-values. This has been incorporated into the model by allowing the layer thickness to be a function of the total interface width as well in a similar sense as the interface width. In order to restrict the amount of fitting parameters, the interface drift is modelled as being equal for both bilayers. The thickness for each layer is therefore described as:

$$\begin{aligned}d_{\text{Ni}} &= D \cdot i + \Gamma \cdot \Lambda \\ d_{\text{Ti}} &= D \cdot i + (1 - \Gamma) \cdot \Lambda\end{aligned}$$

Where D and  $\Gamma$  are dimensionless numbers, i indicates the position of the bilayer in the stack and  $\Lambda$  is the total thickness for the first bilayer. The scattering length density (SLD) for each layer depends both on the elemental composition, and on the density of the layer. The SLD of each bilayer in the sample has therefore been calculated by summing over each element in the layer using the following expression:

$$\text{SLD} = \frac{\rho N_a \sum_{i=1}^N c_i b_i}{\sum_{i=1}^N c_i M_i}$$

Where  $\rho$  denotes the volumetric mass density of the layer and  $N_a$  is Avogadro's number. The elemental concentration in the layer, the scattering length and the molecular weight for each element are described by  $c_i$ ,  $b_i$  and  $M_i$  respectively. The density for each bilayer has been calculated with a linear interpolation using the bulk densities for each element. The structural properties of the samples are fitted for within a reasonable range from the expected values given the XRR and NR data.



## Results and Discussion

TEM measurements on both samples show smooth interfaces throughout the multilayer. While some roughness correlation can be observed, any obvious roughness accumulation is not present in either of the samples. Bright field TEM micrographs are shown in figure X. Some crystallinity can be observed for the  $^{11}\text{B}_4\text{C}$  doped sample...

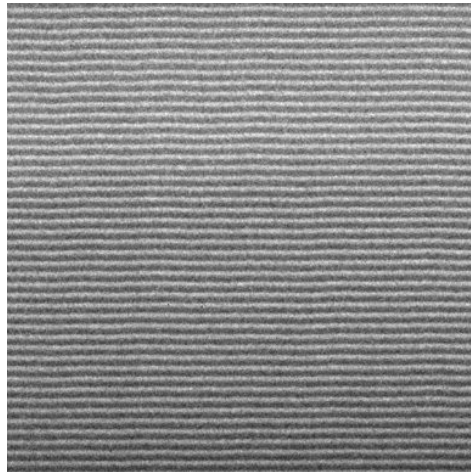


Figure 1: Idea is to have IFM18008 and IFM18009 side by side, this is just one of them.

Figure X shows the experimental XRR and NR measurements, as well as a simulated fit to the specular data. The off-specular signal can be seen in the insets in the right-hand corner. The theoretical model has been fitted to the XRR and NR data simultaneously using and is in excellent agreement with the experimental data. The structural parameters that follow from these fits show an average interface width of 4.5 Å for the sample that has been co-deposited with  $^{11}\text{B}_4\text{C}$ . This is a clear improvement over the samples deposited with pure Ni/Ti, which have an average interface width of 6.3 Å at the first bilayer with an accumulation of 0.03 Å per bilayer. This amounts to a total increase in interface width of 3 Å over the entire multilayer. An interface drift of X Å per bilayer can be observed as well in both measurements.

It can be observed that the samples with  $^{11}\text{B}_4\text{C}$  have a stronger diffuse signal than the pure samples. This may be attributed to a lower intermixing between the subsequent layers, leading to a stronger signal from roughness correlation between the layers. Furthermore, the pure Ni/Ti sample shows clear signs of oxidation both in the TEM measurements, as well as in the fitted simulations, whereas the sample that has been co-deposited with  $^{11}\text{B}_4\text{C}$  didn't show any signs of oxidation at all.

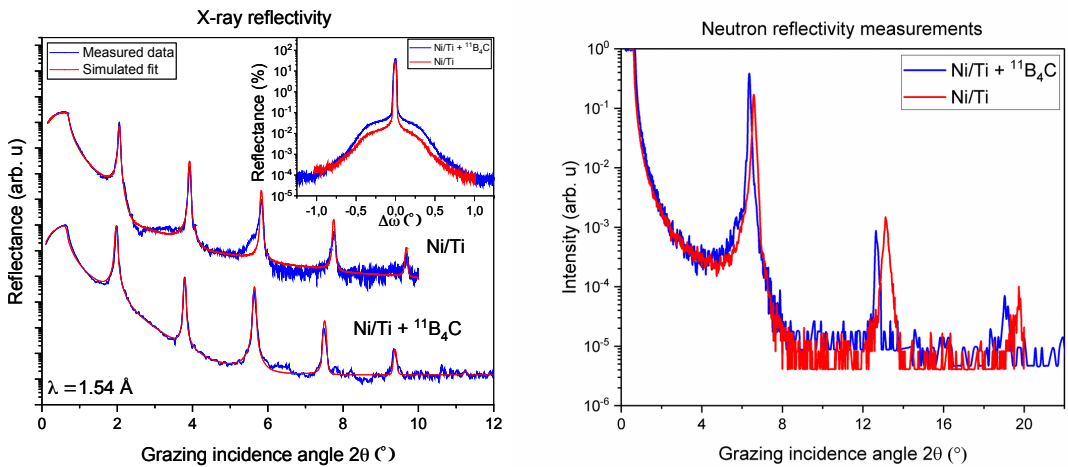
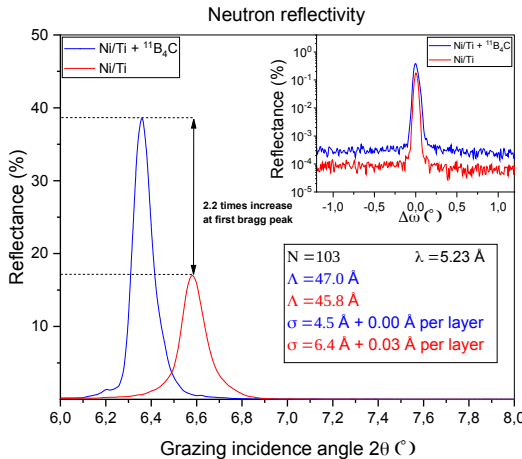
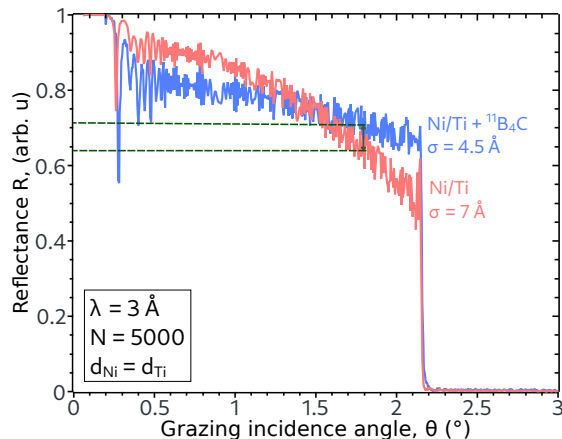


Figure XX shows a linear comparison of the neutron reflectivity at the first Bragg peak for these two samples. The sample that has been co-deposited with  $^{11}\text{B}_4\text{C}$  shows a 2.2 times higher reflectance at this position than the pure Ni/Ti sample.



Calculations of predicted neutron reflectivity performance for supermirrors have been done using the IMD software. The same properties have been used as the deposited samples, where the SLD has been calculated using the elemental composition as obtained by ERDA. The multilayers are simulated with an increasing bilayer period from  $X \text{ \AA}$  to XX  $\text{\AA}$ , a neutron wavelength of 3.0  $\text{\AA}$  and a total of 5000 bilayers. The simulated reflectivity performance is shown in figure X. For a typical  $m = 6$  neutron mirror, an increase in reflectance can be observed from 0.64 to 0.72, which amounts to 0.0115 and 0.0374 after 10 reflections for these respective samples, which is an increase of 325% in this particular case.



## **Conclusions**

In this work we investigated a novel magnetron sputter growth technique where  $^{11}\text{B}_x\text{C}$  co-deposition has been combined with a split-bias scheme in order to reduce interface width at Ni/Ti multilayers. Combined fits to experimental XRR and NR data indicate interface widths of 4.5 Å without any accumulated roughness when the sample is co-deposited with  $^{11}\text{B}_x\text{C}$ . This is a significant reduction from the deposited sample with pure Ni/Ti, which show a nominal interface width of 6.3 Å and an accumulation of 0.03 Å per bilayer. This improved interface width offers very good prospects for high-performance supermirrors with high-m values, as well as for neutron instruments for cold neutrons where thinner interface widths are required. Since neutron multilayers are such essential and crucial elements in any intended instrumentation, even the slightest improvement of the performance will have an immediate and large impact on all research using those instruments.

## **Acknowledgements**

Definitely SFF for funding, UU for ERDA measurements. Should SwedNess as a whole be mentioned here?

## **References**

- [11] D.L. Windt, IMD—Software for modelling the optical properties of multilayer films, *Computers in Physics*, 12 (1998).

# Paper II

Include title and authors and stuff.

# Layer Morphology Control in Ni/Ti Multilayer Mirrors by Ion-assisted Interface Engineering and B<sub>4</sub>C Doping

Fredrik Eriksson,<sup>1,\*</sup> Naureen Ghafoor,<sup>1</sup> Sjoerd Broekhuijsen,<sup>1</sup> Daniel Ostach,<sup>2</sup> Grzegorz Greczynski,<sup>1</sup> Norbert Schell,<sup>2</sup> and Jens Birch<sup>1</sup>

<sup>1</sup> Thin Film Physics Division, Department of Physics, Chemistry and Biology (IFM), Linköping University, SE-581 83 Linköping, Sweden

<sup>2</sup> Helmholtz-Zentrum Geesthacht, Centre for Materials and Coastal Research, Institute for Materials Research, Max-Planck-Straße 1, 21502 Geesthacht, Germany

## Abstract

Ni/Ti is the materials system of choice for broadband neutron multilayer supermirrors. The reflected absolute intensity as well as neutron energy range from state-of-the-art mirrors are hampered by a Ni/Ti interface width, typically 0.7 nm (caused by nanocrystallites, interdiffusion, and/or intermixing), limiting the optical contrast across the interface as well as limiting the minimum usable layer thickness in the mirror stack.

In this work we explore elimination of nanocrystallites by amorphization through boron-carbon doping in combination with interface smoothening by modulation of ion-assistance during magnetron sputter deposition of individual Ni and Ti layers, ranging from 0.8 nm to 6.4 nm in thickness.

In situ high-energy synchrotron wide angle X-ray scattering (WAXS) revealed an effective hindering of Ni/Ti crystallization through a minute concurrent B<sub>4</sub>C flux during growth. Post-growth X-ray reflectivity (XRR) confirmed the incorporation of B<sub>4</sub>C but also showed that interface widths deteriorated when a constant substrate bias of -30 V was used. However, XRR showed that interface widths in B<sub>4</sub>C-doped multilayers improved significantly, compared to those in pure Ni/Ti multilayers, by employing a two-stage substrate bias, where the initial 1 nm of each layer was grown with -30 V substrate bias, followed by -100 V bias for the remaining part of the layer.

The present results shows that B<sub>4</sub>C doping of Ni/Ti multilayers leads to significantly smaller interface widths when combined with engineered interfaces through temporal control of the substrate bias. Consequently, a significant improvement of neutron supermirror performance can be expected by employing this technique using <sup>11</sup>B isotope-enriched B<sub>4</sub>C source material.

## 1. Introduction

Neutron scattering is a powerful tool for the study of condensed matter because the wavelengths and energies of thermal and cold neutrons ( $\lambda = 1 - 10 \text{ \AA}$ ) match well to the length and energy scales of solids and liquids [ref]. Thus, there is a lot of information and many interesting phenomena to study using neutron scattering. The applicability of neutron scattering techniques, however, is limited by the relatively low flux of useful neutrons generated by today's research reactors or pulsed spallation sources, which is many orders of magnitude lower than the flux of X-rays produced by contemporary photon sources [ref].

Multilayer mirrors have proved to be key elements for ...

The largest increase in neutron flux to the experiment is expected to come from improving the performance of different neutron optical components [1].

## Ni/Ti neutron multilayer mirrors

Ni/Ti is the materials system of choice for broadband neutron multilayer supermirrors. The reflected absolute intensity as well as neutron energy range from state-of-the-art mirrors are

\*Corresponding author: [freer@ifm.liu.se](mailto:freer@ifm.liu.se)

mobile: +46-707 315 139

hampered by a Ni/Ti interface width, typically 0.7 nm (caused by nanocrystallites, interdiffusion, and/or intermixing), limiting the optical contrast across the interface as well as limiting the minimum usable layer thickness in the mirror stack [2].

Neutron reflectivity theory – few sentences – SLD → Ni/Ti very attractive for neutron multilayer mirrors.

Neutron scattering length densities – large difference in real part, both small imaginary parts → high reflectivity by increasing the number of contributing layers/interfaces.

Layer morphology – roughness and intermixing/interdiffusion limits the performance. State-of-the-art = 7 Å, however improvement on an Å-level yields a significant reflectivity gain.

Even though the state-of-the-art interface width is as low as 7 Å [ref] the interfaces are still in need of special attention. Considering that the reflectivity is exponentially sensitive to the ratio of the interface width to the multilayer period squared, according to the Debye-Waller modification factor [ref], it is clear that even a slight improvement in interface width will have a significant gain in reflectivity. Furthermore, in order to realize higher m-value supermirrors, which require thinner layers to be deposited, the requirements on the interface width becomes increasingly demanding. Considering a neutron waveguide application, where the neutrons are reflected n times and the waveguide transmission depends on each reflection as  $T = R^n$ , the motivation for research on improving the interface definition becomes even stronger [ref]. As a numerical example, decreasing the interface width from 7 Å to 6 Å for a 100 m supermirror waveguide with an average of 14 reflections [ref], designed for m=8 and using a  $z^{-1/4}$  layer thickness distribution [ref] with a minimum layer thickness of d Å, would increase each reflection from X % to Y %, corresponding to an increase in waveguide transmission by as much as Z %.

Supermirror structure? Depth-graded 40 nm→2 nm.

This study explores the possibility to introduce B<sub>4</sub>C into the Ni/Ti multilayer structure and a temporal control of the substrate bias voltage during growth to change the layer morphology and interface definition to improve the neutron reflectivity performance.

[]

### Theoretical considerations

Expected effects of B<sub>4</sub>C doping and substrate bias:

B forms very strong bonds with metals

Predicted enthalpy of formation and enthalpy of mixing of binary Ti and Ni compounds

	Ti $\Delta H_{calc}^{for}$ kJ/mol	Ti $\Delta H_{calc}^{mix}$ kJ/mol	Ni $\Delta H_{calc}^{for}$ kJ/mol	Ni $\Delta H_{calc}^{mix}$ kJ/mol
B	-84	-43	-33	-9
C	-77	-19	+21	+51
N	-146	-35	+36	+86
O	-	-	-244	-
Ni	-52	-35	-	-
Ti	-	-	-52	-35

Strong B-metal bonds limits interdiffusion [3], promotes amorphization [4], however it lowers the necessary adatom mobility required to produce smooth surfaces.

Substrate bias attracts ions from the plasma. Ions  $<\sim 30$  eV surface displacements. Ions  $>\sim 100$  eV causes subsurface implantation.

Make some simple SRIM calculations of this (– to support the chosen values)!

The attracted ions stimulate the adatom mobility without causing any intermixing (using a modulated bias), and provides more dense layers with smooth surfaces.

## 2. Experimental details

Multilayer thin films of pure Ni/Ti and those doped with B<sub>4</sub>C have been deposited onto Si (100) substrates using ion-assisted DC magnetron sputter deposition. The 600-mm-diameter cylindrical deposition chamber is equipped with four 75-mm-diameter sputter sources tilted with an angle of  $\text{X}^\circ$  towards the substrate normal with a target-to-substrate distance of 150 mm. Between adjacent sputter sources high magnetic permeability  $\mu$ -metal shielding is used to minimize cross contamination as well as to extend the magnetic field closer to the substrate. In front of the sputter sources fast-acting shutters allow for control of the sputtered flux and enables single layers, multilayers, as well as co-sputtered layers to be deposited.

The  $10 \times 10 \times 0.5$  mm<sup>3</sup> substrates were rotating around the sample normal at constant rate of 7 rpm, directly in line of sight of all sputter sources. The substrate table was electrically isolated enabling a negative substrate bias voltage to be applied during growth. Although substrate heating was available depositions were performed at ambient growth temperatures ( $< 50$  °C). The chamber was evacuated to a base pressure of  $\text{X}$  Pa ( $\text{Y}$  Torr) using a dual turbo setup and was equipped with a loadlock to maintain a good vacuum and allow for easy sample exchange. The deposition system is described in more detail elsewhere [5].

Ultra-high purity argon gas ( $> 99.999998\%$ ) was introduced to a working pressure of 3 mTorr (0.4 Pa), as measured with a capacitance manometer. Target discharges were established with constant-power power supplies, and discharge powers of 20 W and 60 W, as measured with closed shutters, were used for Ni and Ti, respectively. This yielded Ni and Ti deposition rates of about 0.36 and 0.39 nm/s as determined from hard X-ray reflectivity measurements of single layer films. For B<sub>4</sub>C discharge powers of 0, 17, 35, and 70 W were used.

Both single multilayer structures, with a period of 10 nm and 5 repetitions, and stacked multilayer structures, with periods of 1.6, 3.2, 6.4, and 9.6 nm consisting of correspondingly 32, 16, 8 and 6 repetitions, in order to maintain roughly the same total thickness of each multilayer stack, were deposited. The nominal Ni and Ti layer thicknesses were kept equal. The single multilayer structures have been deposited with two different designs of ion assistance and with different amounts of B<sub>4</sub>C-doping, while for the stacked multilayer structures only the B<sub>4</sub>C-doping was varied. The layer thicknesses were not adjusted for the amount of incorporated B<sub>4</sub>C at different B<sub>4</sub>C target powers and thus the multilayer period increase the more B<sub>4</sub>C that is included. **The composition of the films were evaluated using Elastic Recoil Detection Analysis.**

Either a constant substrate bias voltage of -30 V was applied, or a two-stage modulated substrate bias was employed, where the initial 1 nm of each layer was grown with -30 V substrate bias, followed by -100 V bias for the remaining part of the layer. The latter ion assistance design has proven successful in reducing roughness and eliminating interface mixing in multilayer X-ray mirrors [6], [7].

The deposition system is mounted on a ultra-high load hexapod with high resolution 6-axis positioning at the High Energy Materials Science P07 beamline at PETRA III [5]. This allows fine alignment of the sample with respect to the synchrotron X-ray beam

enabling time-resolved X-ray diffraction data to be acquired during film growth. In situ wide angle X-ray scattering (WAXS) was performed in transmission mode geometry using a 200  $\mu\text{m}$  high  $\times$  700  $\mu\text{m}$  wide X-ray beam at 78 keV, and the diffracted X-rays were collected on a two-dimensional Perkin-Elmer detector at a distance of  $\text{X}$  m from the sample. Each image was acquired for 160 s, corresponding to  $\sim$ 20 turns of full 360° sample revolution, and the images include diffraction information from a 3D volume of reciprocal space.

X-ray reflectivity measurements were performed on Panalytical Empyrean diffractometer using a Cu X-ray tube, a parallel beam mirror with a 1/32° divergence slit on the primary side, and a parallel plate collimator and a collimator slit (0.27°) on secondary side, together with a PIXcel detector in 0D mode. Reflectivity of single Ni/Ti multilayers doped with B<sub>4</sub>C were measured in the range 0°–10° 20 with a step size of 0.01°/step and a collection time of 1.75 s, giving a total measurement time of  $\sim$ 30 minutes.

Reflectivity simulations were performed using the Panalytical X'pert reflectivity software. The optical constants for (pure) Ni and Ti were used for the multilayers grown without added B<sub>4</sub>C, while the optical constants of Ni<sub>80</sub>(B<sub>4</sub>C)<sub>20</sub> and Ti<sub>80</sub>(B<sub>4</sub>C)<sub>20</sub> were used for those containing B<sub>4</sub>C. In all simulations the densities of the layers were however fitted to the critical angle. In the simulations a Gaussian interface broadening, the same for each interface, was included to account for interface roughness and intermixing.

Elemental composition was determined for the samples grown with a constant substrate bias voltage using time-of-flight energy elastic recoil detection analysis (ToF-E ERDA) at the Tandem Laboratory at Uppsala university. A 34 MeV <sup>127</sup>I<sup>8+</sup> primary beam having an incident angle of 67.5° relative to the surface normal was used, and the energy detector was placed at a recoil scattering angle of 45°. A detailed description of the experimental set-up has been given elsewhere [8], [9]. The measured recoil ToF-E ERDA spectra were analyzed using the CONTES code [10], where the measured recoil energy spectrum of each element was converted to relative atomic concentrations.

X-ray photoelectron spectroscopy (XPS) core-level spectra of B 1s, C 1s, Ni... and Ti... were acquired to analyze the chemical bonding structure of boron and carbon atoms within the layers using an Axis Ultra DLD spectrometer operating at a base pressure of  $1.5 \times 10^{-7}$  Pa with monochromatic Al K $\alpha$  radiation ( $h\nu = 1486.6$  eV). In order to avoid uncertainties related to commonly used binding energy scale referencing against C 1s line of adventitious carbon [30], spectra were aligned to the Fermi level cut-off. The spectra were acquired from the  $0.3 \times 0.7$  mm<sup>2</sup> area centered at  $3 \times 3$  mm<sup>2</sup> portion of the sample previously sputter-etched with 0.5 keV Ar ions incident at an angle of 70° from the surface normal. Deconvolution and quantification was performed using the Casa XPS software applying the manufacturer's (Kratos Analytical Ltd.) sensitivity factors [31].

An analytical Tecnai G2 UT FEG microscope operating at 200 kV for a point-to-point resolution of 0.19 nm was used for transmission electron microscopy (TEM) studies. Microstructure and layer definition of Ni/Ti and Ni/Ti doped with B<sub>4</sub>C multilayers were studied using both bright field and dark field imaging as well as high resolution cross-sectional TEM. Dark field imaging was used as an approach to effectively highlight crystalline regions in the sample, while high-resolution TEM was used to investigate the layered structure in the multilayers containing the thinnest periods. The cross-sectional samples were prepared using mechanical grinding and polishing followed by low-energy ion-beam milling using a Gatan precision ion polishing system.

Calculations of predicted neutron reflectivity performance has been carried out using the IMD software [11].

SRIM calculations [ref] of Ar ion bombardment of Ni and Ti bilayers, based on the chosen ion assistance growth parameters, support the observed interface phenomena.

### 3. Results and Discussion

Wide angle X-ray scattering measurements performed after growth on the stacked multilayers are presented in Figure 1. The detector size and distance from the sample allows diffraction from atomic plane distances  $>X$  nm to be recorded using 78 keV photons. This corresponds to observing diffraction from the Ni (111) and (002), and Ti (110) and (002) atomic planes, if present. Most of the recorded diffraction spots, however, originate from the crystalline Si substrate and the Al<sub>2</sub>O<sub>3</sub> sapphire viewing window, marked in Figure 1 by circles and triangles, respectively.

In Figure 1 a) the 2D X-ray diffraction pattern of a stacked Ni/Ti multilayer grown without B<sub>4</sub>C-doping and using a uniform ion assistance by applying a -30 V bias voltage is shown. Apart from substrate and window reflections, strong Ni 111 and faint Ti 002 reflections are visible, showing that the layers under these conditions grow crystalline. Other film reflections are too weak to be observed. Furthermore, since these are diffraction spots, rather than rings, the crystallites are oriented with respect to the substrate. With the Ni 111 in the growth direction and Ti 002 at 45° from the growth direction, the Ni layers are 111 textured while the Ti layers have a 110 texture, as commonly observed for an fcc and a bcc metal, respectively, due to a minimization of the surface energies during growth. This is also consistent with other findings for Ni/Ti multilayers presented in the literature [refs].

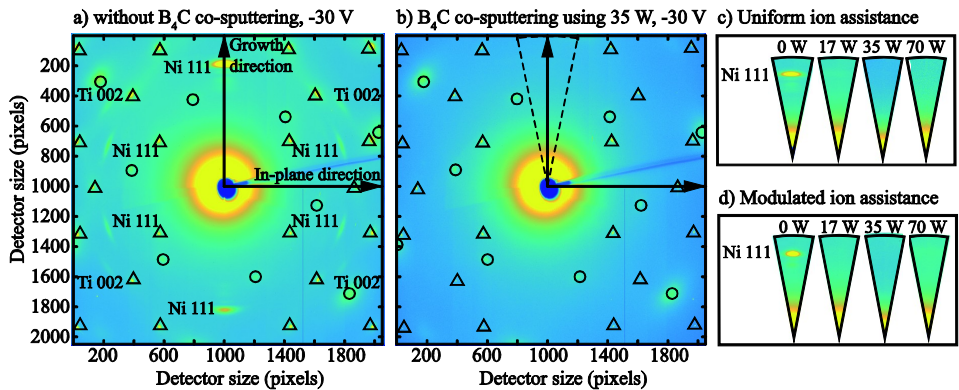


**Figure 1.** Wide angle X-ray scattering a) without B<sub>4</sub>C co-sputtering, b) B<sub>4</sub>C co-sputtering using a magnetron power of 35 W, and c) influence of different B<sub>4</sub>C powers on the Ni 111-formation in the growth direction.

For growth under the same conditions, except for the addition of B<sub>4</sub>C to the multilayer by co-sputtering (using a 35 W magnetron power), diffraction neither from Ni or Ti is observed, as can be seen in the image in Figure 1 b), and the multilayer is considered to be X-ray amorphous. In fact, any addition of B<sub>4</sub>C, from the lowest to the highest applied magnetron power, causes the multilayers to be X-ray amorphous, irrespective of the used ion assistance design, as seen from the absence of the Ni 111 reflection in the region around the growth direction in Figures 1 c) and d). Without the addition of B<sub>4</sub>C the Ni 111 reflection is present although more well-defined when using a modulated ion assistance, indicating a stronger 111 texture in this case.

Although not clearly visible in the images in Figure 1 c) and d), multilayer reflections are present inside the Ni 111 diffraction spots along the growth direction, showing the presence of a multilayered structure perpendicular to the substrate normal, both for a uniform and a

modulated ion assistance. The reflections are however too few and diffuse to be used to accurately determine the multilayer periods in these stacked multilayers.

In Figure 2 the cross-section of the stacked multilayers, corresponding to those discussed above in Figure 1 a) and b), are shown in bright-field, dark-field and high-resolution TEM micrographs. The nominal multilayer periods are indicated in the bright-field micrograph.

When studying the micrographs for the multilayer grown without  $B_4C$  and using a uniform ion assistance in Figure 2, it is seen in a) that the layers are more rough for larger multilayer periods, that the roughness increases with thickness within each multilayer stack, and, for the two thicker periods, that the Ti-on-Ni interface is more rough than the corresponding Ni-on-Ti interface. The asymmetric interface widths for Ni/Ti multilayers have previously been reported in the literature [refs].

From the dark field micrograph in b), the thicker layers are clearly crystalline as seen from the bright regions in the two upper multilayers. The high-resolution micrograph in c) of the thinnest multilayer periods close to the substrate shows that there are crystallites formed also in these thin layers. In addition, the high-resolution micrograph shows that there is no layered structure present.

#### Explain these observations here:

Larger periods allow faceted Ni and Ti crystallites to grow larger, increasing the interface width. **Intermetallics formed at the interfaces.** The accumulating roughness can be explained by... crystallite formation, **kinetic roughening due to an insufficient adatom surface mobility**... while the asymmetric interfaces are due to a **forward knock-on effect**.... and a **difference in displacement energies(?)** for Ni and Ti. Diffusion of Ti in Ni..? Probably not diffusion, since the adatoms do not have sufficient kinetic energy. These observations have been made also by other researchers [refs].

The observations of crystalline layers, absence of periodicity in thin period multilayers, formation of interface intermetallics, and an accumulating interface roughness with total multilayer thickness, summarize very well the main features limiting the neutron reflectivity performance of Ni/Ti multilayers.

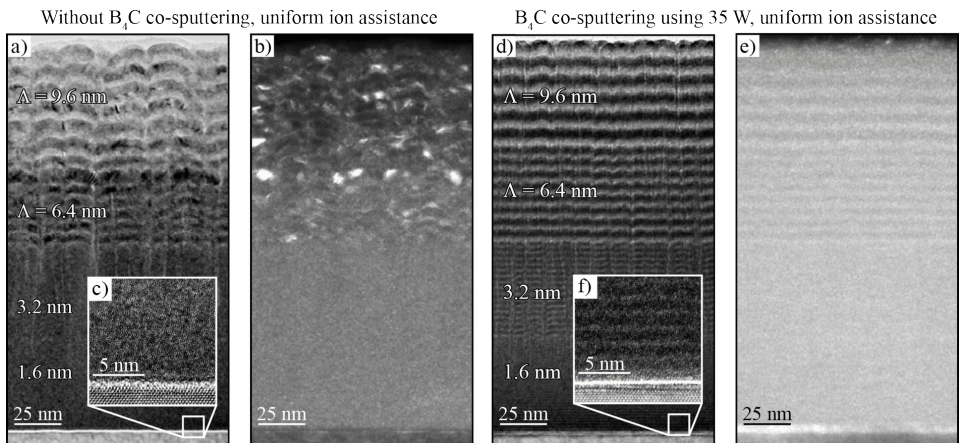


**Figure 2.** Evolution of crystallinity in stacked Ni/Ti multilayers grown with and without  $B_4C$  co-sputtering and a constant ion assistance. a) Bright field micrograph, b) dark field micrograph, c) high-resolution micrograph of a Ni/Ti multilayer grown without  $B_4C$ . d) Bright field micrograph, e) dark

field micrograph, and f) high-resolution micrograph of a Ni/Ti multilayer grown using 35 W B<sub>4</sub>C co-sputtering.

When introducing B<sub>4</sub>C into the Ni/Ti multilayer, Figure 2 d), e), and f), the structure changes significantly. Most obvious is the reduction of the accumulated roughness in d) and the complete absence of any crystallites in f). The high-resolution micrograph of the thinnest layers confirms the formation of an amorphous layer structure throughout the multilayer stack but also that there is a chemical modulation visible for periods as short as 1.6 nm.

**Explain these observations here**

The amorphization by introducing B and C in to the structure is... due to...

*Petrov et al. Microstructural evolution during film growth, J. Vac. Sci. Technol. 2003:*  
Low-energy ion irradiation during growth is used extensively to overcome the characteristically rough and under-dense microstructures of refractory materials deposited at low Ts (typically Ts/Tm<0.25) [refs]. Under the correct set of deposition conditions, ion bombardment has been shown to increase nucleation rates and film density, to decrease average grain size, to inhibit the formation of columnar structures associated with high surface roughness, and to controllably affect the defect density and orientation of coatings.

[12]

In Figure 3 bright field TEM micrographs of single multilayer structures with a 10 nm periodicity and 5 repetitions are shown in two different length scales to provide both a close-up view and a larger overview of the structures. The crystalline layers with faceted crystallites, and intermetallics at the interfaces are again observed in Figure 3 a) when no B<sub>4</sub>C is added and a uniform ion assistance is used. Using B<sub>4</sub>C co-sputtering and a constant ion assistance in b), the layers are amorphous but there is an accumulating roughness present indicating that the applied substrate bias voltage results in insufficient adatom mobility leading to a kinetically limited growth. With B<sub>4</sub>C co-sputtering and using a modulated substrate bias voltage, with a higher voltage in the end of each layer, shown in c), the layers are amorphous and smooth, and there is no significant accumulated roughness. The improved interface definition using a combination of B<sub>4</sub>C co-sputtering and a modulated ion assistance is clearly shown in the overview micrographs in the top of Figure 3.

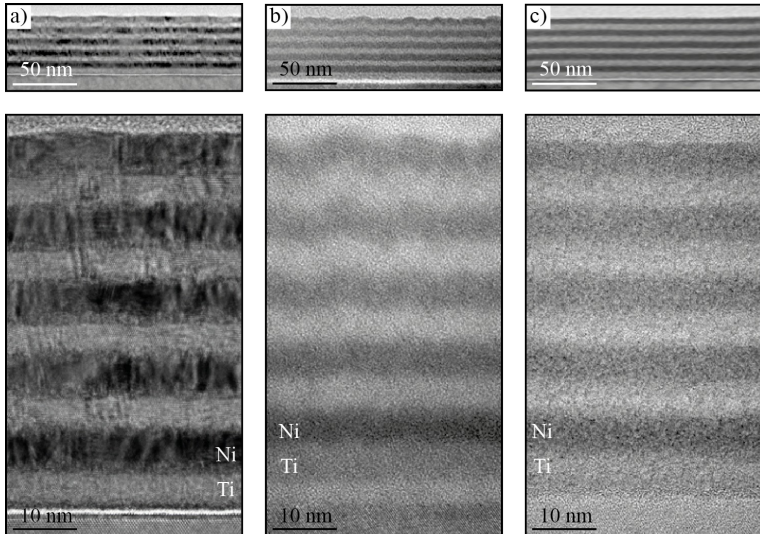


**Figure 3.** Bright field TEM micrographs of single Ni/Ti multilayers showing the effect of ion assistance. In a) no B<sub>4</sub>C is added and a constant ion assistance is applied during growth, while in b) 35 W B<sub>4</sub>C co-sputtering is used with a constant ion assistance, and in c) 35 W B<sub>4</sub>C co-sputtering and a modulated substrate bias voltage is applied. Overview micrographs are shown on top.

From the wide angle X-ray scattering measurements it was found that the multilayers were X-ray amorphous for all investigated B<sub>4</sub>C concentrations. To investigate the influence of the amount of B<sub>4</sub>C on the interface quality hard X-ray reflectivity measurements and fitting were employed. In Figure 5 X-ray reflectivity measurements are shown for periodic multilayers, similar to those presented in Figure 3, grown with different ion assistance and increasing B<sub>4</sub>C magnetron powers. Since the position of the Bragg peaks are related to the period of the multilayer, the peak shifts towards smaller grazing incidence angles with increasing B<sub>4</sub>C magnetron powers shows that an increasing amount of B<sub>4</sub>C is being incorporated. For both a constant and a modulated ion assistance the periods increase linearly from about 9.7 nm to about 11.5 nm, i.e. by almost 19 %, when increasing the B<sub>4</sub>C magnetron power up to 70 W.

Since the reflectivity profiles represent the Fourier transform of the electron density variation along the growth direction, more and sharper Bragg peaks qualitatively correspond to more well-defined interfaces that are more abrupt and flat, and the regular appearance of Kiessig fringes is an evidence of a high layer thickness uniformity.

When using B<sub>4</sub>C co-sputtering and a constant ion assistance it can be seen from the reflectivity measurements in Figure 5 a) that there are fewer Bragg peaks with lower intensities and more irregular Kiessig fringes when the amount of B<sub>4</sub>C in the multilayer is increased. Thus, even though the multilayers turn amorphous, the B<sub>4</sub>C doping deteriorate the multilayer structure. This is due to an effective reduction of the adatom mobility by formation of more metal boride and carbide bonds when increasing the amount of B and C atoms in the multilayer, in combination with an insufficient ion assistance due to a too low ion energy. The low adatom mobility cause interface roughness which can not be counteracted by the applied substrate bias voltage.

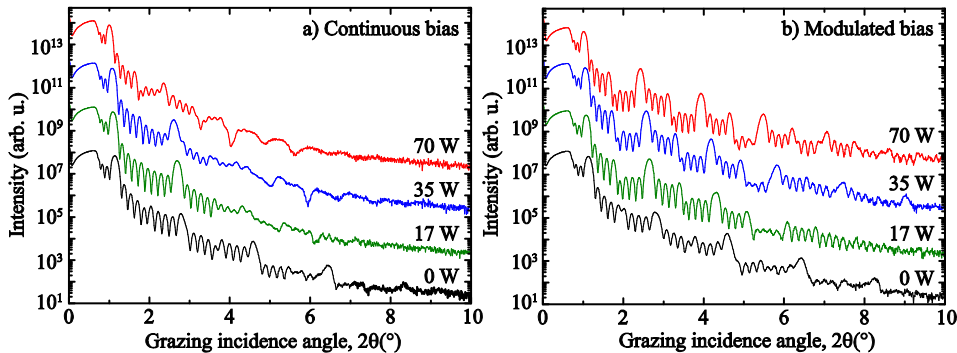


**Figure 4.** X-ray reflectivity measurements of multilayers grown using a) a constant ion assistance, and b) a modulated ion assistance. Vertically shifted for clarity.

When applying a modulated ion assistance with a higher ion energy in the end of each layer the resulting interface morphology evolution with increasing amount of B<sub>4</sub>C incorporation is completely different. Without addition of B<sub>4</sub>C (0 W magnetron power) the reflectivity profiles are almost identical. However, with increasing B<sub>4</sub>C the trend is now instead towards more Bragg peaks with higher intensities and more clear Kiessig fringes, indicating improved interface qualities with more B<sub>4</sub>C.

The low ion energy assistance in the beginning of each layer allows for the formation of an abrupt, although rough and porous, initial part of each layer, while the higher ion energy in the end of each layer provides forward knock-on densification and an increasing adatom surface mobility for a smooth top surface for the deposition of the next layer [ref Ni/V].

Thus, as seen from these results, when B<sub>4</sub>C co-sputtering is used for layer amorphization, a modulated ion assistance is not only beneficial for the interface structure, but is in fact necessary for the formation of ... high quality multilayers.

Use SRIM (or the analytical calculations) to verify the chosen bias voltages – see what happens with these voltages/energies.

To confirm the qualitative observations made above fittings were made to the measured reflectivity profiles to quantitatively obtain the individual interface widths of Ni and Ti for the different growth conditions. Although an accumulating roughness is evident from the transmission electron microscopy studies, the same interface width have been applied throughout the multilayer stack in the simulations, effectively resulting in an overestimated average interface width. The results are illustrated with the interface width as a function of the B<sub>4</sub>C magnetron power in Figure 5 a) for constant ion assistance and in b) for a modulated ion assistance, respectively.

The interface width is always smaller when using a modulated ion assistance, also without B<sub>4</sub>C incorporated in the multilayer.

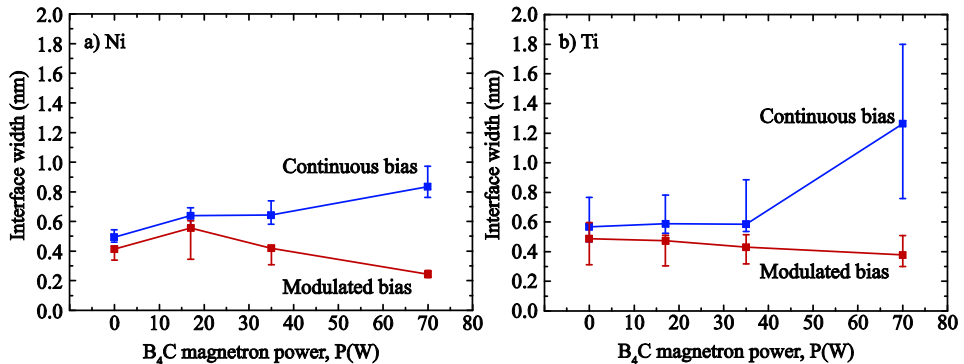


**Figure 5.** Interface width evolution with increasing  $B_4C$  magnetron power.

$B_4C +$  modulated assistance  $\rightarrow$  significantly reduced interface widths.

### XPS

Due to the mixing caused by the Ar(?) sputtering ions used for depth profiling it is not possible to extract any interface width.

In the depth profile of the multilayer grown with a 70 W magnetron power  $B_4C$  co-sputtering, it was found that the average B/C ratio is 4.3 for the top multilayer period.

The different depth scales are due to different sputtering yields for the etching. Without  $B_4C$  the sputtering rate is 6.5 Å/min, while with  $B_4C$  the sputtering rate is reduced to 4.9 Å/min. This indicates that the sputtering yield has decreased with B and C in the layers, indicating the formation of metal boride and carbide bonds, that have higher surface binding energies than for the pure elements.

Chemical shift for the Ni 2p photoelectron peak towards higher binding energies inside the Ti layer shows Ni implanted into Ti (during depth profiling, or during deposition?) Similarly for the Ti 2p peak.

Ti-B bonds inside the Ti layer. C-B bonds inside the Ni layers. Compare enthalpies of formation..

C-Ti inside Ti layer.

Brasklapp: Some residual C implanted into Ni and Ti due to Ar+ etch  
Some TiC and NiC formed due to Ar+ etch.

**Figure 6.** X-ray photoelectron spectroscopy results -depth profiling + chemical shifts representing the metal boride and carbide bonding...

These numbers can be used to predict the performance of the neutron reflectivity performance.

### Predicted performance of Ni/Ti-based supermirrors

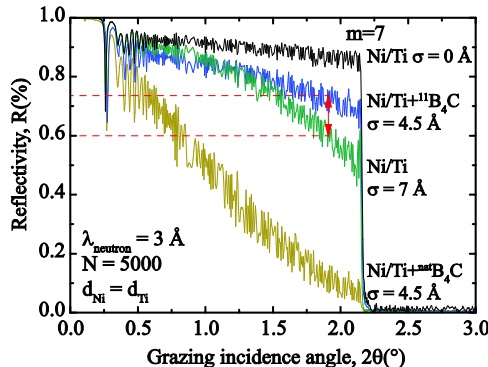


**Figure 7.** Supermirror performance

Significantly increased waveguide transmission expected with Ni/Ti+11B4C. Good prospects for long, high reflectivity, high-m, supermirrors for waveguides.  
Ta med fler än Ni/Ti, NiTiB4C, ...?

## 4. Discussion

### 4.1 Film growth and microstructure

### 4.2 Evolution of crystallinity in Ni/Ti multilayers

### 4.3 Neutron optical properties

Here in this work we have only used a low number of layers in order to investigate the concept of B4C-doping and ion-assisted growth to improve the interfaces. [...] We should mention **stress-reduction** with amorphous Ni/Ti multilayers. This enables more layers to be deposited, and thus facilitates supermirrors with higher m-values.

B<sub>4</sub>C + modulated assistance → significantly reduced interface widths.

Hard X-ray reflectivity simulations indicate interface widths of about 4.5 Å

When looking closer at the interfaces in Figure 6 c) they are very smooth, but they seem to be quite intermixed.

Reducing the intermixing could thus lead to a further improvement in interface quality.

Could it be that the 100 eV ion bombardment in the end of each layer is too large, causing a forward knock-on effect leading to interface mixing?

## 5. Conclusions

Here the concept for layer morphology control using B4C in Ni/Ti multilayer mirrors have been

Ni/Ti with B4C → X-ray amorphous

Pure Ni/Ti multilayers are crystalline and have a 111 texture. Using a modulated bias voltage the texture is stronger.

## Acknowledgements

Mit VR?

## Captions

Figure 1. XRD diffractograms for cubic CrN deposited at 600, 650 and 700 °C. a) The gas flow is set to 21 sccm nitrogen and 33 sccm argon (40% nitrogen) resulting in single phase CrN. The inset is a pole figure for cubic CrN deposited on sapphire at 700 °C. b) The gas flow is set to 11 sccm nitrogen and 33 sccm argon (20% nitrogen) resulting in the formation of hexagonal Cr<sub>2</sub>N.

Figure 2.

Figure 3.

## **Figures**

## References

- [1] D. Liu, B. Khaykovich, M.V. Gubarev, J. Lee Robertson, L. Crow, B.D. Ramsey, D.E. Moncton, Demonstration of a novel focusing small-angle neutron scattering instrument equipped with axisymmetric mirrors, *Nat Commun*, 4 (2013) 2556.
- [2] T. Veres, S. Sajti, L. Cser, S. Bálint, L. Bottyán, Roughness replication in neutron supermirrors, *Journal of Applied Crystallography*, 50 (2017) 184-191.
- [3] S.a. Bajt, Improved reflectance and stability of Mo-Si multilayers, *Optical Engineering*, 41 (2002).
- [4] N. Ghafoor, F. Eriksson, A. Aquila, E. Gullikson, F. Schafers, G. Greczynski, J. Birch, Impact of B4C co-sputtering on structure and optical performance of Cr/Sc multilayer X-ray mirrors, *Opt Express*, 25 (2017) 18274-18287.
- [5] J.L. Schroeder, W. Thomson, B. Howard, N. Schell, L.A. Naslund, L. Rogstrom, M.P. Johansson-Joesaar, N. Ghafoor, M. Oden, E. Nothnagel, A. Shepard, J. Greer, J. Birch, Industry-relevant magnetron sputtering and cathodic arc ultra-high vacuum deposition system for in situ x-ray diffraction studies of thin film growth using high energy synchrotron radiation, *Rev Sci Instrum*, 86 (2015) 095113.
- [6] F. Eriksson, N. Ghafoor, F. Schafers, E.M. Gullikson, J. Birch, Interface engineering of short-period Ni/V multilayer X-ray mirrors, *Thin Solid Films*, 500 (2006) 84-95.
- [7] F. Eriksson, F. Schafers, E.M. Gullikson, S. Aouadi, N. Ghafoor, S. Rohde, L. Hultman, J. Birch, Atomic Scale Interface Engineering by Modulated Ion Assisted Deposition Applied to Soft X-ray Multilayer Optics, *Applied Optics*, DOI (2008).
- [8] H.J. Whitlow, G. Possnert, C.S. Petersson, Quantitative mass and energy dispersive elastic recoil spectrometry: Resolution and efficiency considerations, Elsevier, Nuclear Instruments and Methods in Physics Research Section B: Beam Interactions with Materials and Atoms, 27 (1987) 448-457.
- [9] J. Jensen, D. Martin, A. Surpi, T. Kubart, ERD analysis and modification of TiO<sub>2</sub> thin films with heavy ions, *Nuclear Instruments and Methods in Physics Research Section B: Beam Interactions with Materials and Atoms*, 268 (2010) 1893-1898.
- [10] M.S. Janson, CONTES, Conversion of Time-Energy Spectra, a program for ERDA data analysis, Internal Report, Uppsala University, DOI (2004).
- [11] D.L. Windt, IMD—Software for modeling the optical properties of multilayer films, *Computers in Physics*, 12 (1998).
- [12] W. Li, J. Zhu, H. Li, Z. Zhang, X. Ma, X. Yang, H. Wang, Z. Wang, Ni layer thickness dependence of the interface structures for Ti/Ni/Ti trilayer studied by X-ray standing waves, *ACS Appl Mater Interfaces*, 5 (2013) 404-409.